JGR Oceans

RESEARCH ARTICLE
10.1029/2021JC017691

On the Processes Sustaining Biological Production in the Offshore Propagating Eddies of the Northern Canary Upwelling System

Elisa Lovecchio[1,2], Nicolas Gruber[1], Matthias Münnich[1], and Ivy Frenger[3]

[1]Environmental Physics, Institute of Biogeochemistry and Pollutant Dynamics, ETH Zurich, Zürich, Switzerland, [2]Ocean BioGeosciences, National Oceanography Centre, European Way, Southampton, UK, [3]GEOMAR Helmholtz Centre for Ocean Research Kiel, Kiel, Germany

Key Points:

- The pattern of biogeochemical tracers and production is determined by trapping and isolation in cyclones and by stirring in anticyclones
- Vertical small-scale mixing drives the nutrient supply in mature eddies while the vertical advective flux downwells nutrients
- Eddy regenerated production dominates over new production highlighting the intense recycling of the organic material exported offshore

Correspondence to:
E. Lovecchio,
elisa.lovecchio@noc.ac.uk

Citation:
Lovecchio, E., Gruber, N., Münnich, M., & Frenger, I. (2022). On the processes sustaining biological production in the offshore propagating eddies of the northern Canary Upwelling System. *Journal of Geophysical Research: Oceans*, *127*, e2021JC017691. https://doi.org/10.1029/2021JC017691

Received 17 JUN 2021
Accepted 20 JAN 2022

Author Contributions:
Conceptualization: Elisa Lovecchio, Nicolas Gruber
Data curation: Elisa Lovecchio
Formal analysis: Elisa Lovecchio
Funding acquisition: Nicolas Gruber
Investigation: Elisa Lovecchio, Nicolas Gruber, Matthias Münnich, Ivy Frenger
Methodology: Elisa Lovecchio, Nicolas Gruber, Ivy Frenger
Project Administration: Nicolas Gruber, Matthias Münnich
Software: Elisa Lovecchio, Matthias Münnich, Ivy Frenger
Supervision: Nicolas Gruber, Matthias Münnich
Validation: Elisa Lovecchio, Nicolas Gruber, Ivy Frenger
Visualization: Elisa Lovecchio

Abstract Oceanic mesoscale eddies constitute ephemeral hotspots for marine life and are pivotal for the lateral transport of nutrients and organic matter. Here, we use a high-resolution coupled physical-biogeochemical model to study the processes sustaining biological production and export in long-living cyclonic (CE) and anticyclonic (AE) eddies of the northern Canary Upwelling System (CanUS). We track the eddies for 18 months as they propagate offshore, and study their composite properties in time in a Lagrangian manner. Our model shows that long-living CEs sustain their production with the nitrogen that they initially trap in the nearshore nutrient-rich waters and keep isolated in their cores. The vertical input of nitrate from below tends to be comparatively small, and is mostly driven by mixing. In contrast, AEs tend to start with low nutrient concentrations in their core as they do not trap coastal waters, but have elevated concentrations at their periphery. In AEs, stirring is responsible for both the building up of the positive nitrate anomaly at depth and the enhanced lateral input of organic nitrogen in the near-surface. Compared to CEs, the input of nitrate into the euphotic zone by vertical mixing is substantially more important. Though regenerated production dominates in both types of eddies, new production is higher than the regional average in CE cores and at the rim of AEs, partially compensating for the intense losses due to sinking. Both cyclonic trapping and transport and anticyclonic stirring shape the regional pattern of organic matter and nutrients in the northern CanUS.

Plain Language Summary Mesoscale eddies are ubiquitous rotating flow structures in the ocean with a diameter of 20–200 km. They are hot-spots of productivity and contribute to the lateral transport of nutrients. Through the use of ocean simulations, we studied the nutrient dynamics in long-living cyclonic (counter-clockwise rotating) and anticyclonic (clockwise rotating) mesoscale eddies that are formed near the north-western African coast and propagate westward into the subtropical North Atlantic. We find that biological activity in both types of eddies rely mostly on the local recycling of the already present organic matter, and that the supply of new nutrients is sustained by small-scale vertical mixing of nutrients from below. High nutrient concentrations in the center of cyclonic eddies are in most part trapped during the eddy formation and preserved for a long time thanks to their lateral isolation from the surrounding water. Anticyclones, which are characterized by lower nutrients in the center compared to the eddy periphery, are strongly influenced by lateral stirring of the high nutrient levels at depth and by the subsequent vertical mixing of nutrients into the sun-lit ocean layer.

1. Introduction

Oceanic mesoscale eddies are ubiquitous structures that constitute an extraordinary laboratory to study the connection between marine physics, biogeochemistry, and biology (Falkowski et al., 1991; Mahadevan, 2014; McGillicuddy, 2016). In spite of their relatively small size that spans from a few tens to a few hundreds of kilometers, mesoscale eddies represent an intrinsic mode of flow of the ocean (Chaigneau et al., 2009; Faghmous et al., 2015), with substantial impact on the lateral transport of momentum and material properties (Ito & Marshall, 2008; Thompson et al., 2014). Even though these structures modulate biological activity in the global ocean (McGillicuddy, 2016; NASA-OBPG, 2015), achieving a full understanding of the plethora of processes that regulate biology in mesoscale eddies has remained elusive. This is largely a consequence of the ephemeral nature and high spatio-temporal variability of these structures, and the complexity of the physics that governs them.

Writing – original draft: Elisa Lovecchio
Writing – review & editing: Elisa Lovecchio, Nicolas Gruber, Matthias Münnich, Ivy Frenger

Satellite-based observations of sea surface height (SSH) and surface chlorophyll have constituted an important source to develop a better description of the general properties and diversity of mesoscale eddies on a global scale (Chelton, Schlax, & Samelson, 2011; Frenger et al., 2018; Fu et al., 2010; Gaube et al., 2014). Further, in situ studies and modeling efforts provided insights regarding the three-dimensional structure of the eddies (Chaigneau et al., 2011; Pegliasco et al., 2015). Formed by baroclinic and barotropic instabilities induced by shear in coastal currents or flow disturbance by obstacles such as islands (Marchesiello et al., 2003; Sangrà et al., 2009), eddies have been shown to live for as long as several years and to drift away from their region of origin for hundreds of kilometers with the typical translational velocity of a Rossby wave (Chelton et al., 2007; Frenger et al., 2015; Klocker & Abernathey, 2014). While propagating westward on average, these structures rotate around their center with speeds that exceed by several times their translational velocity, potentially trapping water and tracers in their core (Chelton, Schlax, et al., 2011).

On the large scale, the lateral and vertical redistribution of tracers by eddy processes can determine the dynamics and biological activity of entire ocean regions (Amores et al., 2017; José et al., 2016; Lachkar et al., 2016; Qiu & Chen, 2005; Zhang et al., 2014). While fueling marine production (Klein & Lapeyre, 2009; Oschlies & Garçon, 1998), eddies impact the lateral and vertical export of organic matter (Chenillat et al., 2016; Mahadevan, 2014; Nagai et al., 2015) and determine the distribution of nutrients and production in upwelling regions (Barton et al., 1998; Gruber et al., 2011; Lachkar & Gruber, 2011). In the oligotrophic regions adjacent to upwelling systems, eddies constitute important tracer reservoirs containing roughly 1/3 of the available organic matter of the euphotic layer (Lovecchio et al., 2018). Satellite-based and modeling studies have highlighted both regional differences in the large scale impact of mesoscale eddies and differences in the specific role of cyclonic eddies (CEs) and anticyclonic eddies (AEs) in modulating biogeochemistry (Chenillat et al., 2016; Gaube et al., 2014; McGillicuddy, 2016; Nagai et al., 2015).

On the small scale, a variety of biophysical interactions taking place within mesoscale eddies has been identified thanks to increasingly high-resolution observations and models. At the early stages of their life, eddy intensification drives a long-lasting shoaling (deepening) of the isopycnals in the core of CEs (AEs; Siegel et al., 1999), inducing shallower (deeper) vertical mixing in CE (AE) cores (Dufois et al., 2016). The resulting doming of the isopycnals in the eddy cores has been associated to a mechanism known as "eddy pumping", assumed to drive upwelling (CEs) or downwelling (AEs) of tracers, although the relevance of this process during the eddy life is debated (Dufois et al., 2016; Lévy, 2003). In the late stages of the eddy life (spin-down phase), the doming of the isopycnals decreases, potentially reversing these vertical fluxes in the eddy cores (Gaube et al., 2014). Trapping at formation strongly influences the eddy properties (Chenillat et al., 2015; Gaube et al., 2014; Moore et al., 2007) and favors the lateral transport of physical and biogeochemical tracers over great distances (Brochier et al., 2014; d'Ovidio et al., 2013; Everett et al., 2015). At the eddy periphery, vertical fluxes induced by ageostrophic flow enhance the vertical advection and mixing of tracers (Koszalka et al., 2010; Mahadevan, 2016; Zhong et al., 2017) through both upwelling and downwelling (Klein & Lapeyre, 2009; Martin & Richards, 2001; Zhong & Bracco, 2013). Lateral stirring by eddies affects the horizontal gradients of tracers, creating dipole-like anomalies and transferring spatial variability from large to small scales (Abraham, 1998; Mahadevan & Campbell, 2002; Chelton, Gaube, et al., 2011). Eddies modulate the local trophic structure of plankton communities, favoring species co-existence and shifts toward larger cells (Laiolo et al., 2016; McGillicuddy et al., 2007; Vaillancourt et al., 2003).

Despite the recent progress in identifying this variety of eddy processes, their relative role in modulating the pattern and evolution of the biogeochemical properties of the eddies is still not understood (José et al., 2014; Mahadevan et al., 2008). Two points require special attention. First, the degree of lateral isolation of the eddy interior from its surrounding environment remains uncertain, with contradictory results from in situ and modeling studies (Everett et al., 2015; José et al., 2017; Karstensen et al., 2015, 2017). Second, the dominant process driving the vertical supply of nutrients and organic matter in eddy cores has remained elusive (McGillicuddy, 2016). Several potential processes have been identified to drive this supply (Gaube et al., 2015; Mahadevan, 2014; McGillicuddy & Robinson, 1997): This includes the vertical displacement of the isopycnals at the formation of eddy, continuous mesoscale vertical advection during the eddy life, up- or downwelling generated by eddy-wind interaction, and ageostrophic sub-mesoscale fluxes.

In the present article, we analyze and quantify the physical and biogeochemical processes that drive and maintain biological productivity and nutrients in long-living eddies of the northern Canary Upwelling System (CanUS),

one of the four major Eastern Boundary Upwelling Systems (EBUS) and one of the most productive continental margins (Carr, 2002; Carr & Kearns, 2003; Mackas et al., 2006). The northern CanUS is located along the north-western African coast between Cape Blanc (21°N) and Cape Beddouza (32.5°N), contains the southward flowing Canary current (CC) and is characterized by intense mesoscale activity (Pelegrí et al., 2005; Sangrà, 2015). Mesoscale eddies in this system have been shown to contain about 30% of the entire organic carbon stock in the offshore euphotic layer and to transport this organic matter offshore beyond more than 1,500 km from the coast (Lovecchio et al., 2018). This transport substantially impacts the carbon and nitrogen budgets of the eastern subtropical North Atlantic, which otherwise is an oligotrophic region. As a region with high mesoscale activity and steep biological-biogeochemical gradients from the productive east to the oligotrophic west, the northern CanUS constitutes therefore a well-suited setting to investigate the processes that shape and support biological activity in mesoscale eddies.

2. Methods

2.1. Numerical Model Setup

We employ the UCLA-ETH version of the Regional Ocean Modeling System (Shchepetkin & McWilliams, 2005) coupled with the Nutrient Phytoplankton Zooplankton Detritus (NPZD) ecosystem model of Gruber et al. (2006). The model configuration (grid, forcing, boundary conditions) is identical to that used in Lovecchio et al. (2017) and further evaluated by Lovecchio et al. (2018). A specialty of the employed setup is the Atlantic telescopic grid, which covers the entire Atlantic Basin and is characterized by a strong grid refinement toward the north-western African coast (Figure 1). This grid allows us to resolve mesoscale variability in the region of interest (northern CanUS) with a resolution between 4.7 km at the coast and 18 km offshore, while modeling the circulation of the entire Atlantic, thus avoiding the lateral boundary condition problems that affect regional setups. We define the northern CanUS as the portion of the EBUS that is crossed by the alongshore flow of the CC and is located along the north-western African between Cape Blanc (21°N) and Cape Beddouza (32.5°N; Figure 2).

The NPZD ecosystem model is nitrogen-based with nitrate (NO_3^-) and ammonia (NH_4^+) being the two limiting nutrients. Their sum is equal to dissolved inorganic nitrogen (DIN), thus DIN = $[NO_3^-] + [NH_4^+]$. Particulate organic nitrogen (PON) is defined as the sum of the nitrogen contained in phytoplankton, zooplankton, small detritus, and large detritus. Our model does not explicitly simulate a dissolved organic matter pool, but as discussed by Lovecchio et al. (2017), the impact of this limitation on the results is moderate, since the small detritus pool shares many similarities with the dissolved pool. These small detritus particles are primarily formed by the mortality of phytoplankton and sloppy feeding of zooplankton. Owing to their slow sinking speed (1 m day^{-1}), they can be transported, like dissolved organic matter, over long distances before they leave the euphotic zone. In contrast, the fast-sinking large detritus particles (sinking speed of 10 m day^{-1}) remain in the euphotic zone for only a few days. These particles are formed from the feces of zooplankton and from the coagulation of small particles. While sinking, both detritus pools are subject to remineralization. Given the fixed C: N stoichiometric ratios of 106:16 assumed in the model for organic matter production and decomposition, all biological nitrogen fluxes have directly corresponding carbon fluxes.

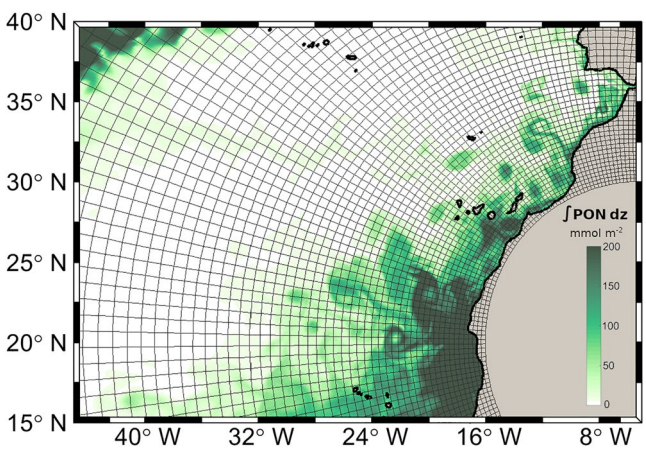

Figure 1. Atlantic telescopic grid zoomed around the northern CanUS region [21°N, 32.5°N]. The plot shows every 5th grid line. Background: bi-daily mean of the vertically integrated modeled particulate organic nitrogen (PON) on 10-11/02/31 of the climatological simulation.

The model is forced from the atmosphere with monthly mean climatological wind stress, solar shortwave radiation, and fluxes of freshwater and heat, all taken from the ERA-Interim reanalysis (Dee et al., 2011). We ran the model for a total of 53 yr, which include an initial spin-up of 29 yr, followed by 24 yr of analysis run. For the present study, we used the 24 yr of model output in the form of bi-daily means, which allowed us to have enough statistics of the eddies in the region of study. On top of the physical and biogeochemical quantities (temperature, salinity, velocities, and tracer concentrations), we output the bi-daily means of selected fluxes calculated at model run time. These fluxes are: New production (NP) and regenerated production (RP); net community production (NCP); PON sinking flux; and the mixing fluxes of PON and DIN. The vertical advective fluxes of PON and DIN are calculated offline as the product of the vertical velocity and the tracer concentrations. As our model is forced from the atmosphere by prescribed wind stress, it

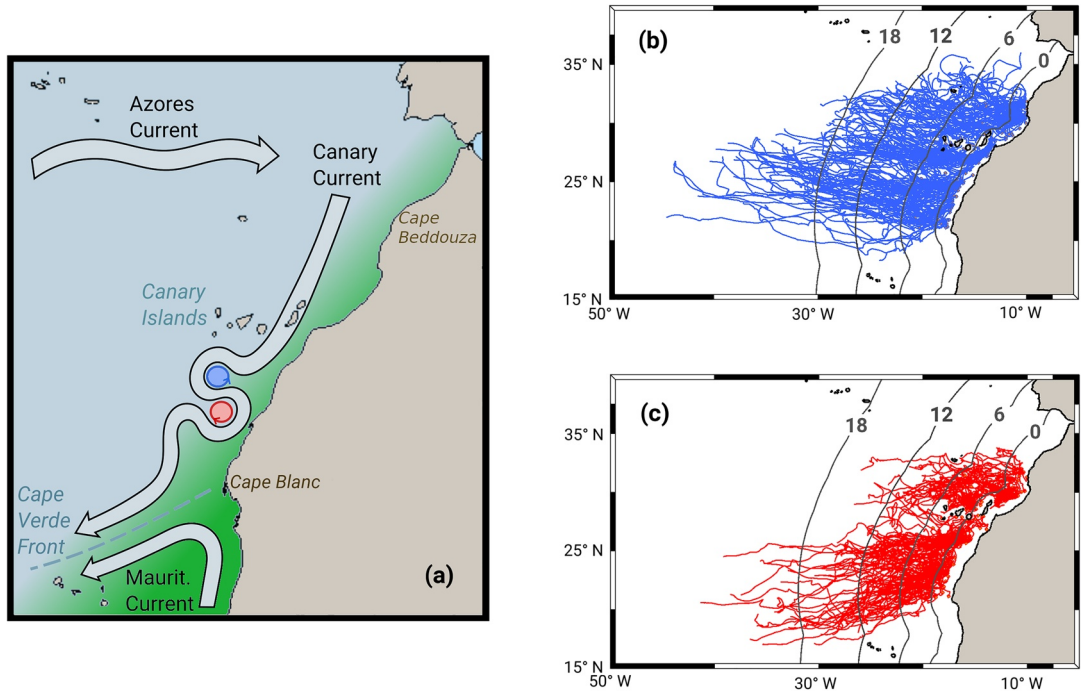

Figure 2. (a) Schematic of the formation mechanism of nearshore-generated CEs and AEs by meandering of the coastal Canary current and of the regional system of currents; color shading illustrates the mean regional pattern of tracers such as DIN and PON, with green representing higher concentrations. Tracks of long-living eddies (>6 months) for (b) CEs and (c) AEs in the northern CanUS plotted until their 18th month of life, and showing the north-west drift of CEs and south-west drift of AEs. Isolines in subplots (b and c) indicate the mean age of eddies (in months) at each offshore distance.

does not account for the potential interactions between the eddies and the overlying wind, which can contribute to the vertical transport of nutrients and organic matter in the core of the eddies (Gaube et al., 2015; McGillicuddy, 2016). We will discuss the implications of this model limitation in the discussion section.

2.2. Model Evaluation

The model is performing well in the northern CanUS sector, corresponding to our focus region (see the Taylor diagram in Appendix Figure A1 including the references to the employed data sets in its caption, as well as Lovecchio et al., 2018, 2017). Modeled sea surface temperature (SST) and sea surface salinity (SSS) have a very high correlation with the observations, and the biases of the long-term mean SST and SSS are less than 0.5°C and 0.2°C, respectively. Surface chlorophyll and its offshore gradient also match the observations in the whole northern CanUS. The model simulated vertically integrated net primary production (NPP) represents the observed estimates with regard to both pattern and seasonality, with a low bias that affects mostly latitudes south of 25°N. The pattern and magnitude of the modeled standard deviation of SSH and eddy kinetic energy (EKE) are very similar to those derived from satellite data. A model high bias in EKE in the nearshore may well be explained by the inability of satellites detect narrow upwelling filaments, that are most abundant in the nearshore region. Satellite products also struggle to represent coastal EKE which is strongly driven by wind stress (Renault et al., 2016).

For this study, it is important that the model faithfully simulates long-living eddies. We, therefore, summarize here the evaluation of the modeled eddy field presented in Lovecchio et al. (2018), while further evaluation of the eddy tracks is provided in the following dedicated Section 2.4. The model reproduces well the numbers of large eddies that are detected from satellite products (>50 km radius), with a slight low bias. In terms of surface, CEs and AEs cover, respectively, 15% and 10% of the CanUS domain, summing up to ~25% of the area, in agreement with Chaigneau et al. (2009). In line with satellite data, the fractional area covered by eddies is maximum at 250 km offshore and decreases thereafter more sharply for AEs than for CEs.

2.3. Eddy Detection and Tracking

To identify CEs and AEs in our bi-daily output, we employed the SSH-based eddy detection algorithm described by Faghmous et al. (2015). For each eddy, we required a minimum size of 9 grid points. Owing to the telescopic nature of our grid, this resulted in varying minimum sizes of our eddies with increasing offshore distance, ranging from a minimum mean diameter of about 15 km near the shore of northwestern Africa to about 60 km at the edge of our analysis region. As our focus is on long-living eddies that tend to be on the larger end of the spectrum, this changing minimum size has little impact on our results. For each bi-daily mean, we saved the location of all the eddy centers as well as the coordinates of the surface grid points occupied by the each detected eddy.

Eddy tracks were built using a nearest-neighbor search algorithm. Two AEs found at time step t and at time step $t + 1$, were identified as the same AE at different times (and therefore as belonging to the same track) if the center of the AE found on time step $t + 1$ was apart less than a search distance D_{sr} from the center of the AE found on time step t (and likewise for CEs). The search distance D_{sr} of about 17 km per each 2-day mean time step was estimated as an upper limit from the average Rossby wave speed (Chelton, Schlax, et al., 2011). A tolerance of 2 days was used in this track building process, in order to reconnect the broken tracks: If a matching eddy was not found on time step $t + 1$ the algorithm looks for an eddy also on time step $t + 2$ in a radius of $2 \cdot D_{sr}$. If then an eddy was found on time step $t + 2$, the missing eddy on time step $t + 1$ was substituted by a virtual flagged eddy, with no associated area or center location. If no eddy was found at $t + 2$, the algorithm repeats the search at $t + 3$ in a $3 \cdot D_{sr}$ range, potentially adding 2 virtual eddies to the track. If no eddy was found at $t + 3$, the track was considered to have ended.

2.4. Track Selection and Composites Calculation

We base our Lagrangian analysis on 271 CE tracks and 201 AE tracks of long-living eddies that originate in the nearshore (defined as the first 500 km from the northern CanUS coast) and last for more than 6 months (Figures 2b and 2c). These long-living tracks account for 23% and 20% of all the CE and AE tracks generated in the same nearshore region and living more than 1 month. Although these percentages are twice those found worldwide by Chelton, Schlax, et al. (2011) for tracks of analogous duration, the cited study may underestimate long lived eddies with small amplitudes in upwelling systems (Faghmous et al., 2015). Track properties, such as the equatorward drift of AEs and poleward drift of CEs and their mean propagation speed (Figure 2) correspond to those found in observation-based studies (Chelton, Schlax, et al., 2011; Morrow et al., 2004). In addition, the pattern of the identified tracks closely corresponds to that found from the analysis of satellite products for the same region of study (Pegliasco et al., 2015). Note that since virtual flagged eddies are discarded, the effective total number of CEs and AEs used for the analysis may oscillate slightly along the mean eddy track lifetime (see Appendix, Figure A2a).

The spatial pattern of the eddy imprint on biogeochemical tracers can reveal processes at play. In order to study this pattern, we created Lagrangian composites of the CEs and AEs at intervals of a few months from the eddy formation, that is, we averaged the eddy properties at different intervals of time according to the time since first detection, which we interpret here as eddy age. We note that for multiple reasons we do not scale the eddy age by the eddy's lifetime, as done in other publications (Frenger et al., 2015; Samelson et al., 2014). First, given the relative constant westward propagation speed, an absolute lifetime perspective retains the information of the approximate geographical position of the eddy (see Figures 2b and 2c, Appendix Figure A2b). This is important since the biogeochemical environment varies strongly with the offshore distance. Second, the death of the eddies in our analysis mostly occurs by eddies interaction with topography, other eddies, and frontal systems, such that the eddy life time is primarily determined by external factors and not by the eddies spinning down. Analyzing the results in terms of a relative eddy life age would thus tend to distort the results.

For all eddy composite calculations, anomalies of the physical and biogeochemical variables for each time window were obtained as differences from the climatological bi-daily values, computed by linearly interpolating the adjacent monthly climatological means. Anomalies were calculated on the original model grid before any regridding or averaging.

We built 2D and 3D composites of the eddy evolution along the tracks. To lower the computational costs of regridding tens of thousand of eddies, we limited the number of calculations by building 2D and 3D composites to the first available time window (2-day mean) of each month of the eddy's life. Thus, rather than showing monthly

averages, the plotted eddy composites represent snapshots that are representative of the eddy state at the beginning of the month.

To generate the 2D eddy composites, the 3D tracer fields of the full model domain were first vertically integrated up to a reference depth on the original model grid, or, in the case of vertical fluxes, sliced at the reference depth. The tracer fields were then co-located with each eddy, rescaled, and regridded onto a 2D regular grid of 3×3 eddy diameters. For the 3D composites, we regridded the full 3D structure of each eddy on a normalized 3D grid of dimension 3×3 eddy diameters by 300 m depth without any vertical rescaling. For each eddy type and selected eddy age separately, the resulting normalized 2D and 3D eddy fields were then averaged.

Based on the shape of the mean composite tracer fields compared to the identified eddy radii, we find that the eddy identification-algorithm underestimates the size of the eddies at the moment of their formation (see Appendix, Figure A3). This may be due to the fact that young eddies interact with coastal upwelling filaments near the coast, which may lead to a strong initial deformation of the eddies. Fortunately, this mismatch only occurs in the first month after the eddy formation. Plots of the eddy composites at any later stage indicate that the eddy boundary is well captured by the algorithm, that is., the maximum geostrophic velocities of the eddy composites are well aligned with the perimeter of the normalized eddy. Due to this shortcoming, we will discuss only results past the first month of the eddy's life, when the average structure is well defined and correctly identified by the algorithm.

2.5. Lagrangian Budgets of Inorganic and Organic Nitrogen

To analyze the origin, transformation, and fate of DIN and PON in the euphotic layer (100 m depth) of the tracked eddies, we calculated the average tracer concentrations and tracer fluxes inside the eddy core and rim region for each 2-day mean of the eddies' life. To avoid any interpolation errors these budget calculations were performed on the original grid. The perimeter of the eddy core, that is, the perimeter of the 1R (1 radius) eddy mask, was determined from the contour identified by the algorithm for each eddy snapshot belonging to a track. This 1R eddy mask can have an irregular perimeter. We also used a wider 2R (2 radii) mask by expanding the 1R eddy mask by a factor of two in each direction to account also for the rim of the eddy, roughly corresponding to the region in which the eddy rotational speed vanishes. Vertically, we assumed that the eddy occupies exactly the same longitude and latitude grid points at every depth.

For the calculations of the DIN and PON budgets in the euphotic layer of the eddies, we considered the following processes: NCP, that is, the net conversion of DIN into PON as a balance between photosynthetic uptake of nutrients and remineralization of organic nitrogen, vertical sinking flux of PON (VSink), and the vertical advective and vertical mixing fluxes, respectively VAdv and VMix, of both inorganic and organic nitrogen. Vertical mixing fluxes represent in our model those processes that occur on sub-grid scales. Lateral fluxes are calculated as residuals (Res), that is, the difference between the actual derivative of the tracer concentration and the sum of the recorded fluxes, and their magnitude is used to determine the lateral isolation of the eddies. The resulting budget equations for the evolution of the tracer budgets are:

$$\frac{dDIN}{dt} = VAdv(DIN) + VMix(DIN) - NCP + Res(DIN) \quad (1)$$

$$\frac{dPON}{dt} = VSink(PON) + VAdv(PON) + VMix(PON) + NCP + Res(PON) \quad (2)$$

For the final budgets, the tracer concentrations and NCP are vertically integrated over the first 100 m depth (regional mean euphotic layer depth) while physical vertical fluxes are horizontally sliced at the same depth, obtaining 2D fields. The 2D fields are co-located in time and space for each eddy and then averaged over the eddy surface using the 1R and 2R eddy masks. Eddy core budgets (0R–1R range) are calculated using the 1R mask, while eddy rim budgets (1R–2R range) are calculated using a mask obtained as the difference between the 2R and the 1R masks for each eddy. The horizontal averaging, rather than the horizontal integration, gives the same weight to each eddy independently of its size. Finally, mean concentrations and fluxes are averaged throughout all the tracked eddies according to age and type, obtaining the mean evolution of the CE and AE budgets along the eddy tracks.

In contrast to the composite calculations, we calculate monthly mean PON and DIN budgets across the entire time span of each month, that is, averaging across the entire set of bi-daily mean outputs available for every month of interest. This allows us to represent the evolution of the fluxes in time throughout the eddy life. For the summary plot of the average budget of fully developed and stable eddies, we averaged the above-mentioned monthly fluxes between months 4 and 15 of the eddy's life, excluding the first and last 3 months, in order to account for well-formed and stable eddies that have limited interaction with the nearshore upwelling zone.

3. Results

3.1. Physical Evolution of the Eddies

The Lagrangian analysis of the physical structure of the average long-living CEs and AEs is key to understanding the mechanisms driving the evolution of the biogeochemical properties of each eddy type (Figure 3). The eddy physical properties remain very coherent across one and a half years of tracking, despite a decrease in intensity. This decrease is stronger for AEs than CEs: at month 18 the mean composite AE rim is no longer that well defined

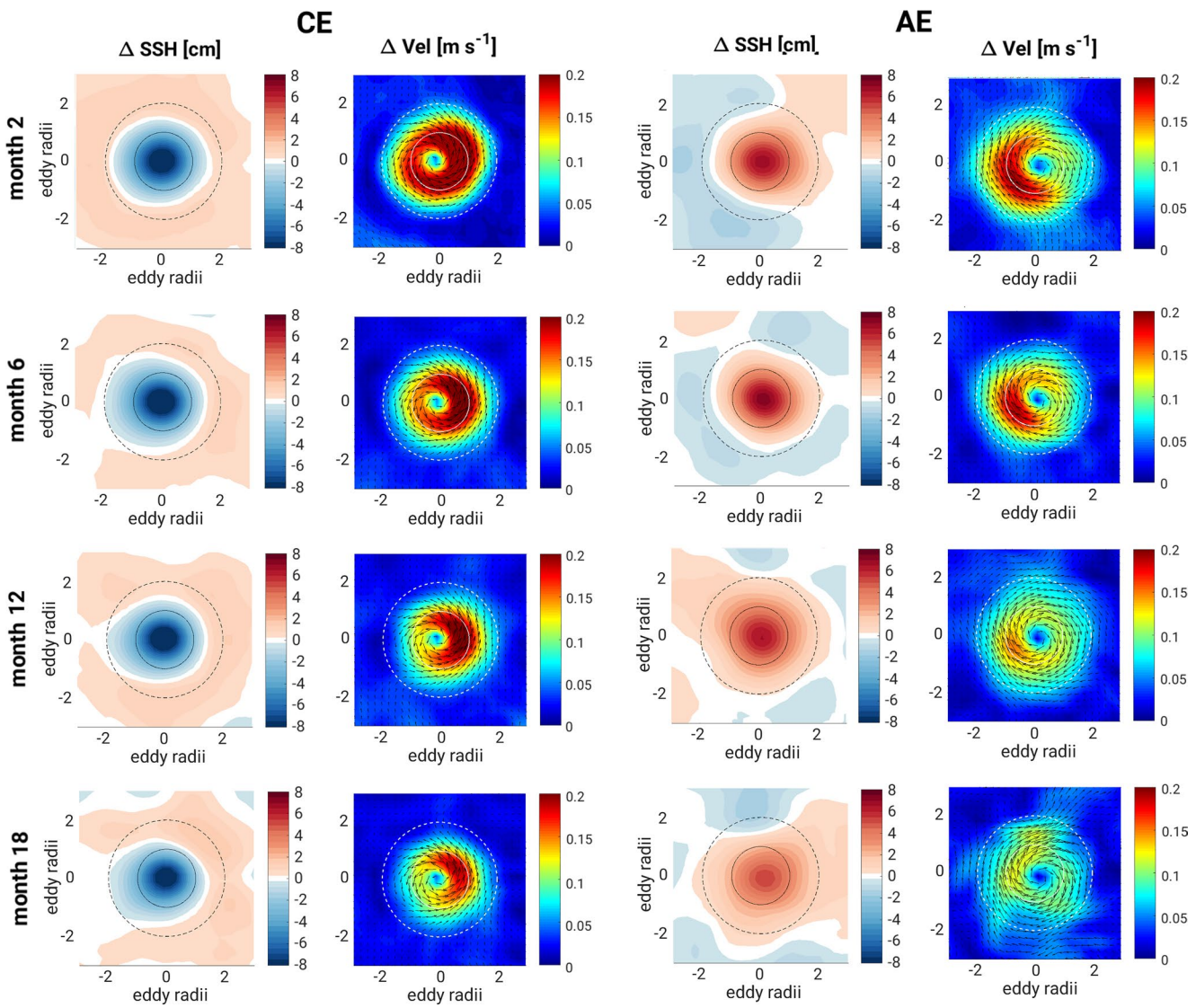

Figure 3. Lagrangian mean evolution of the physical properties of cyclonic (CE, left two columns) and anticyclonic (AE, right two columns) eddies. Rows show snapshots at 2, 6, 12, and 18 months. The first and third columns depict the anomalies of sea surface height (ΔSSH), the second and fourth columns depict the anomalies of the horizontal velocities (ΔVel).

compared to that of the mean CE. This is likely due to the fact that AEs have a tendency to break down more easily than CEs (McWilliams & Yavneh, 1998; Thomas et al., 2013), which also results in a smaller number of averaged AEs compared to CEs at this life stage (see Appendix Figure A2a). The SSH-based eddy-identification algorithm locates the 1R perimeter in correspondence of the maximum rotational speed of the structures, while the 2R perimeter defines well the outermost boundary, where the eddy rotation is still discernible. While the mean eddies are overall rather symmetric, there is a slight E-W asymmetry in the speed of the rotation for both CEs and AEs throughout their life cycle, as previously observed in satellite-based studies and in situ observations (Chaigneau et al., 2011; Liu et al., 2017).

The vertical structure of the mean CE and AE also remains remarkably coherent in our analyzed long-living eddies. Thus, we show here only the vertical structure on month 6 (Figure 4). For both kinds of eddies, anomalies are discernible across the entire water column down to more than 300 m depth, underlining the deep influence of eddies on the structure of the water column. Temperature anomalies (Figures 4a and 4d) are highest in the subsurface at a depth of about 150 m for both young CEs and AEs, in accordance with Pegliasco et al. (2015). The negative temperature anomalies in CEs tend to be stronger in magnitude compared to the positive anomalies for AEs.

The vertical velocities in both CEs and AEs have a dipolar structure, with both an upwelling and a downwelling cell (Figures 4b, 4c, 4e, and 4f). This dipole is consistent with the divergence of the horizontal eddy rotational flow in both CEs and AEs (Figure 3), and is similar to what was found by Barceló-Llull et al. (2017) in an

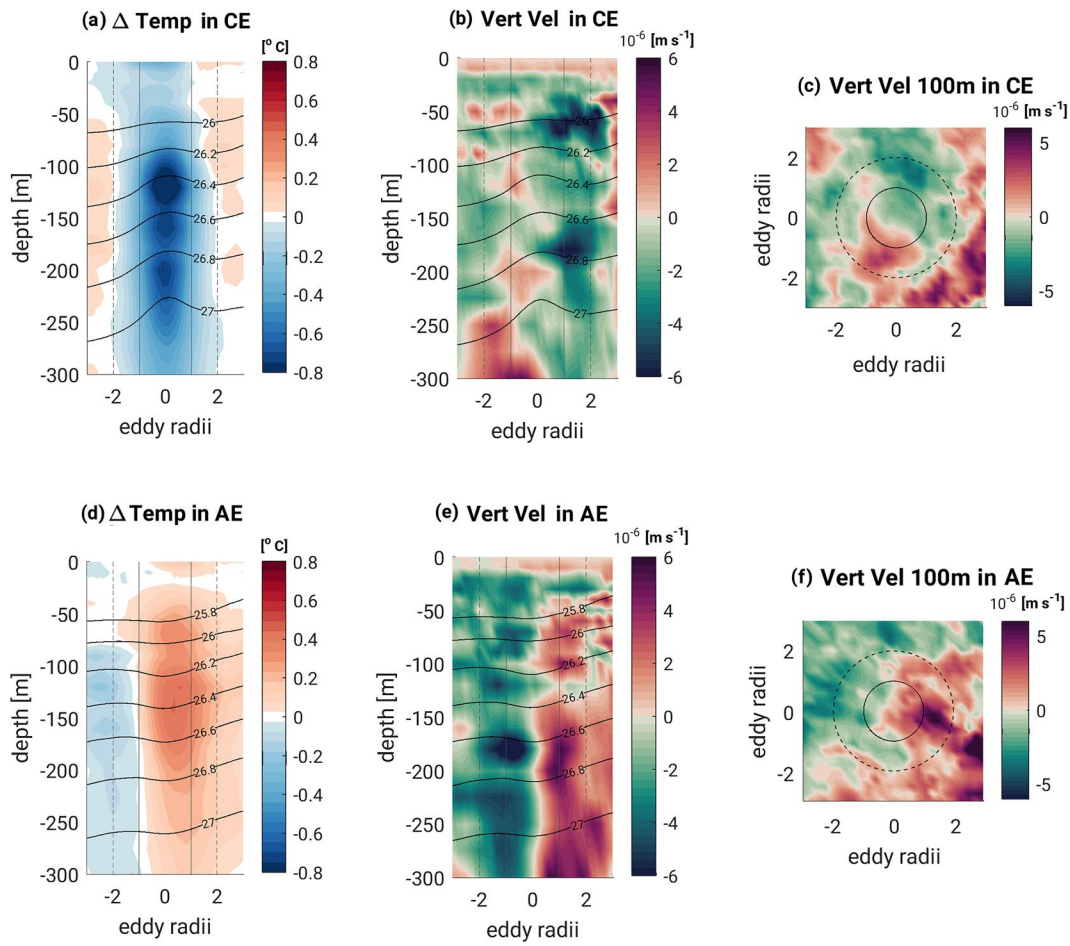

Figure 4. Physical properties of (a–c) the mean cyclonic eddy (CE) and (d–f) the mean anticyclonic eddy (AE) on the first 2-day mean of month 6 of the eddy's life. Shown in panels (a, b, d, and e) are the west-east centered transects of the eddies with black contour lines indicating isopycnals [kg m^{-3}], while panels (c and f) show a horizontal slice of the eddies at 100 m depth. Panels (a and d) show the temperature anomalies (ΔTemp), while (b, c, e, and f) depict the vertical velocity (Vert Vel), with positive values indicating upwelling.

anti-cyclonic mode water eddy (ACME) sampled in the proximity of the Canary Archipelago. ACMEs, however, are characterized by a positive doming of the SSH (analogous to regular AEs) accompanied by an upward tilting of the isopycnals in the near-surface that determines a negative ΔSST and ΔSSS (Schütte et al., 2016). We did not attempt to separate mode water eddies from the surface intensified eddies, but the latter tend to be rare in our model. This is supported by the distribution of the physical properties of the analyzed eddy populations not revealing a clearly distinct sub-group of AEs (nor CEs) in terms of SST-SSS signature (see Appendix: Figure A4). We, therefore, conclude that our eddy composites are representative of regular CEs and AEs, and that this dipolar pattern in the vertical speed is characteristic also of such types of eddies.

3.2. Lagrangian Evolution and Distribution of Organic Nitrogen in the Mean Eddy

While the eddy associated PON stock decreases significantly with time and increasing distance from the coast in both eddy types, the spatial pattern of the PON imprint associated with the eddies remains remarkably constant in each eddy type and differs between CEs and AEs (Figure 5). For the CEs, their high PON stock values over the top 200 m stand out from their surroundings (Figure 5), even in the early phases, when the high values in the

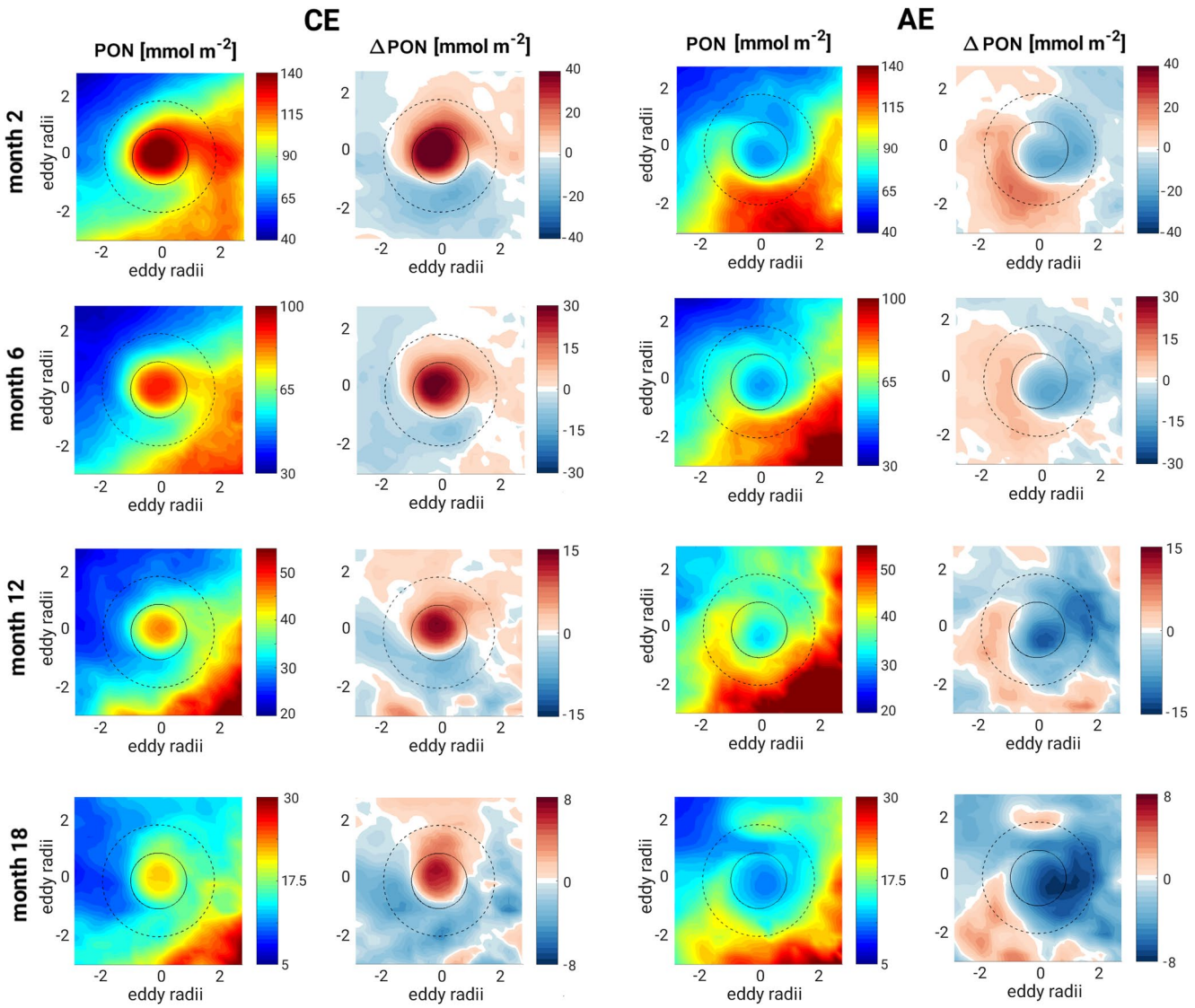

Figure 5. Lagrangian evolution of the PON stock of the top 200 m in the mean cyclone (CE, left two columns) and anticyclone (AE, right two columns). Rows show snapshots at 2, 6, 12, and 18 months. The first and third columns depict the stock, that is, $\int_{-200m}^{0}$PON dz (in the plot simply called PON), while the second and fourth columns show its eddy anomaly with respect to the reference mean (in the plot simply called ΔPON). Note that the range of the colorbars decrease with age.

surrounding waters to the east still mark the presence of the coastal upwelling. In contrast, AE cores show anomalously low PON stock values. As the eddies age, another striking difference between AEs and CEs becomes more evident. At the same ages, the waters surrounding AEs tend to have higher PON stocks than the waters surrounding the CEs, suggesting that the spatial distribution of the AEs is skewed toward more productive regions, and the distribution of the CEs toward lower productive regions. This difference accentuates with increasing age, and is coherent with the north-west drift of CE tracks and south-west drift of AE tracks combined with the regional gradient of tracers, characterized by higher background PON in the south (Figure 2).

In the average CE, an intense positive monopole characterizes the PON stock anomaly, ΔPON, in the eddy core, while in the eddy rim ΔPON is characterized by a weaker dipole structure. AEs have a similar structure of ΔPON, but of opposite sign and with an overall weaker signal. A persistent monopole negative ΔPON can be found in the core of the AEs, while the region between 1 and 2 eddy radii features a dipole. For both types of eddies, the central monopole remains well defined at every life stage, while the positive ΔPON at the rim up to 2 radii from the center becomes smaller in time. This central monopole and peripheral dipole pattern in the ΔPON signature of both CEs and AEs indicates a strong influence of both trapping and stirring of the regional gradient.

For both types of eddies, most of the PON is concentrated in the top 100 m, that is, the productive euphotic layer, where NP and RP are also confined to (Figure 6). However, a significant portion of PON is also found below 100 m. This is primarily the result of vertical export in the form of gravitational sinking as well as downwelling and downward mixing of PON. In terms of anomalies, CEs show a peak of ΔPON that occurs at around 80 m, but positive values can be found well below 200 m highlighting the deep impact of PON export in the core of these eddies (Figures 6a and 6b). In AEs, the positive ΔPON is overall rather homogeneously distributed across depths up to 200 m, with a

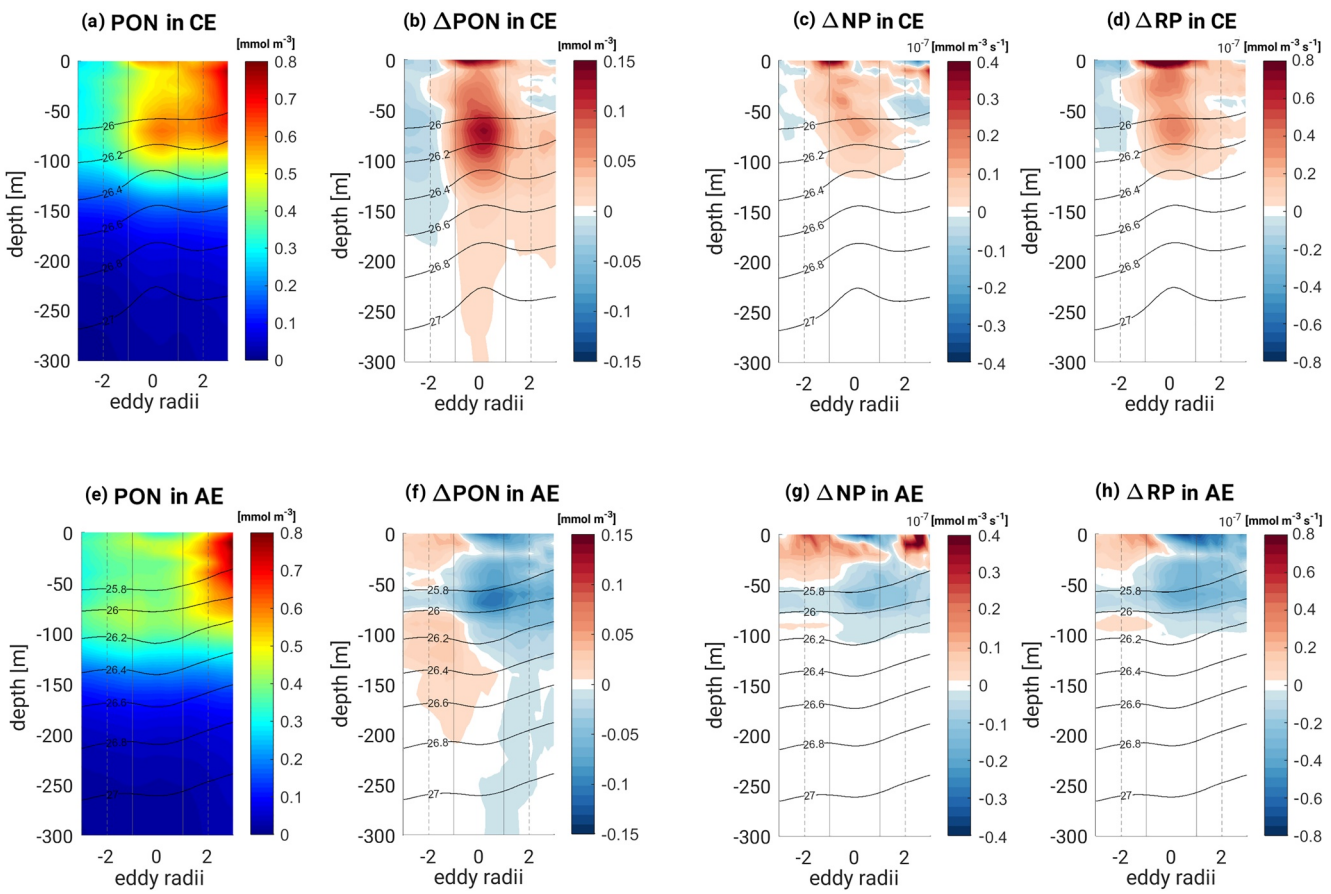

Figure 6. Vertical mean pattern of PON concentration and production in CEs (top row) and AEs (bottom row). The panels depict vertical sections of (a and e) PON; (b and f) the eddy anomaly of PON, that is, ΔPON; (c and g) the eddy anomaly of new production, that is, ΔNP, and (d and h) the eddy anomaly of regenerated production, that is, ΔRP. Shown are west-east centered transects of the mean eddies for the first 2-day mean of month 6 of the eddy's life, with black contour lines indicating isopycnals [kg m^{-3}].

minimum between 50 and 100 m. However, the anomalies tend to be weaker than those of CEs and shifted toward the western periphery of the eddy (Figures 6e and 6f) in agreement with the eddy rim dipole signature.

3.3. Spatial Patterns of Production and Nutrient Concentrations

As for PON, the eddies also show an anomaly in NP and RP. In CEs, the majority of the eddy induced anomalies in new and RP (ΔNP and ΔRP) takes place in the top 10 m and within the eddy core (Figures 6c and 6d). The strongest ΔNP occurs on the western edge of the core, while the shallow maximum is centered for ΔRP. Positive ΔNP and ΔRP extend down to 100 m in the eddy core, and, to a lesser extent, at the eastern rim of the eddy, in analogy to ΔPON (Figure 6b). In AE cores, ΔNP and ΔRP are mostly negative throughout the upper 100 m with a minimum very close to the surface. ΔNP presents also a small positive spike at around 20 m depth in the core. Otherwise, ΔNP and ΔRP match the ΔPON pattern in the first 100 m depth, with positive anomalies on the western side of the eddy (Figures 6g and 6h).

The coherence between the eddy anomalies, that is, ΔNP, ΔRP, and ΔPON, suggest that both regenerated and NP contribute to the anomaly of PON in eddies. For both eddy types, RP dominates and constitutes over 75% of total production in both the rims and cores of the eddies, with a tendency of AE having a slightly larger fraction of RP, consistent with the budget analysis above (see Appendix Figure A5a). Very young CEs show a substantially lower ratio of RP to total production. This means that in these young CEs, the fraction of NP is significantly higher, with an initial maximum of about 50%. However, this fraction quickly decreases during the first 2 months of their life. The initial maximum is likely due to the initial trapping of nitrate-rich upwelled water, which supports a higher ratio of NP (see Appendix Figure A5b). However, after the initial months, the ratio of RP to total production is rather stable in both types of eddies until at least month 15. This is especially striking for cyclones, which largely sustain their high RP ratio while drifting slightly north to regions characterized by lower values of RP.

While the distributions of nitrate, NO_3, and ammonia, NH_4, in the CEs and AEs differ from those of PON, the eddy anomalies in nitrate, ΔNO_3, and ammonium, ΔNH_4, have clear similarities with ΔPON (Figure 7). The doming of the isopycnals in the CEs is associated with anomalously high nitrate concentrations in the center of eddy, leading to a distinct positive ΔNO_3 at the bottom of the euphotic zone around 100 m depth (Figure 7b). Likewise, ΔNH_4 also shows a distinct maximum in the center of the CEs, although with a shallower and more confined distribution than ΔNO_3. For the AEs, the center region of the eddies are depleted in NO_3 down to about 200 m. Below this depth the anomalies switch sign, with the central part of the AE having a surplus of NO_3 that seem to intrude from below the western side of the eddy at shallower depths, resulting in a distinct east to west increase in ΔNO_3 (Figure 7f). AEs also show a peripheral dipole in NH_4, combined with a mild positive anomaly in the core below 100 m (Figure 7h), in analogy to the PON anomaly.

The correspondence between the anomalies in PON and ammonia is expected. NH_4 is the product of the local remineralization of PON, hence its abundance is directly tied to the abundance of PON. For ΔNO_3, the argument is opposite, since PON is the product of the photosynthetic uptake and reduction of nitrate. Differences also occur owing to the photosynthetic uptake of ammonia and the regional pattern of NO_3 concentrations that increase at depth. Note that the maximum anomalies of new and RP are located significantly shallower in the water column compared to the deep-reaching nutrient anomalies. This is mostly due to light limitation, which confines NP and RP to the upper 100 m, that is, to the mean depth of the euphotic layer in the region. Further differences arise from the fact that production tends to drive down the nutrients.

The elevated nutrient levels in the CEs provide the basis for considerably higher NP and RP compared to AEs. In both eddy types, the dominant ammonia-fueled RP rejuvenates the organic matter pool of the long-living eddies through the local recycling of both coastal materials trapped at formation and PON produced in the eddies at later times. Nitrate-fueled NP, instead, allows the eddy to substitute the organic material that has sunk out of the mixed layer with newly formed PON and has therefore a very important role in the preservation of the PON anomaly. Throughout the life of the eddy, NP must be fueled by an adequate amount of NO_3, either constituting part of the DIN trapped at formation or supplied by either vertical or lateral input during the eddy life. Interestingly, the shapes of the nitrate anomalies for CEs and AEs differ substantially: in CEs, the eddy core hosts the most intense positive anomaly, which decreases at depth; in contrast in AEs the pattern of ΔNO_3 is asymmetric and intensifies at depth, with a positive maximum on the western side of the eddy. A detailed look at the processes at play in the

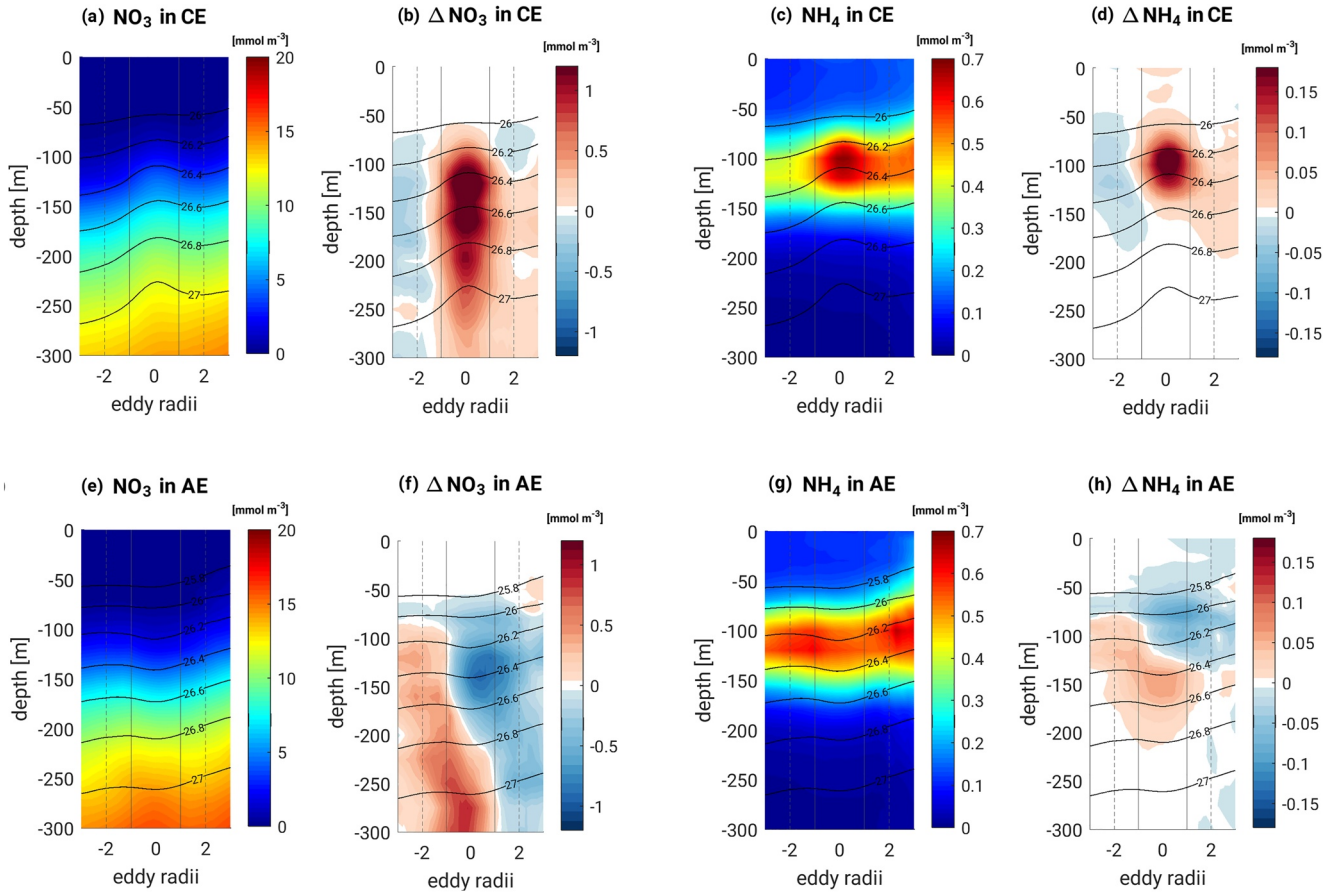

Figure 7. Same as Figure 6 but for (a and e) nitrate (NO_3); (b and f) the eddy anomaly of nitrate, that is, ΔNO_3; (c and g) ammonia (NH_4), and (d and h) the eddy anomaly of ammonia, that is, ΔNH_4.

build-up of the distinct ΔNO_3 patterns in CEs and AEs can provide an understanding of the different processes fueling NP in the two types of eddies.

3.4. Sustaining New Production: Physical Fluxes Driving the NO_3 Anomaly

In order to explain the shape of the deep-reaching NO_3 anomalies in both CEs and AEs, we study the horizontal and vertical NO_3 fluxes at the boundary of the euphotic layer (100 m depth) and below (Figure 8). In CEs, horizontal advective fluxes of nitrate maintain a radial symmetry (Figure 8a) both in the euphotic layer and, even more clearly, below (100–200 m range), transporting the tracer cyclonically around the center of the eddy without strong evidence of a lateral inflow. This radial symmetry suggests an important role of the efficient combined mechanism of trapping and isolation of the NO_3-rich upwelled waters in CE.

In AEs, instead, lateral fluxes of NO_3 show both a lateral accumulation and an inflow of nitrate on the south-eastern side across the 2R perimeter, suggesting that NO_3 gets caught within the 2R perimeter of the AE (Figure 8c). This influx and the resulting west-east asymmetry of NO_3 is a result of the anticyclonic rotation and the large scale gradient of nutrients in the offshore region of the CanUS (Figure 2a). The continuous stirring of the regional gradient of NO_3 in AE is especially relevant as these eddies, while moving westward, drift slowly southward (Figure 2c), therefore approaching the most nutrient rich offshore waters of the CanUS and traveling along the sharp horizontal nutricline of the Cape Verde front.

In trying to explain, the deep-reaching signature of the eddy NO_3 anomalies, we must also consider vertical fluxes. However, the vertical advective fluxes of NO_3 (Figures 8b and 8d) do not match nor seem to explain the patterns of NO_3 in the two types of eddies. While potentially deep-reaching, the dipolar shape of these fluxes results

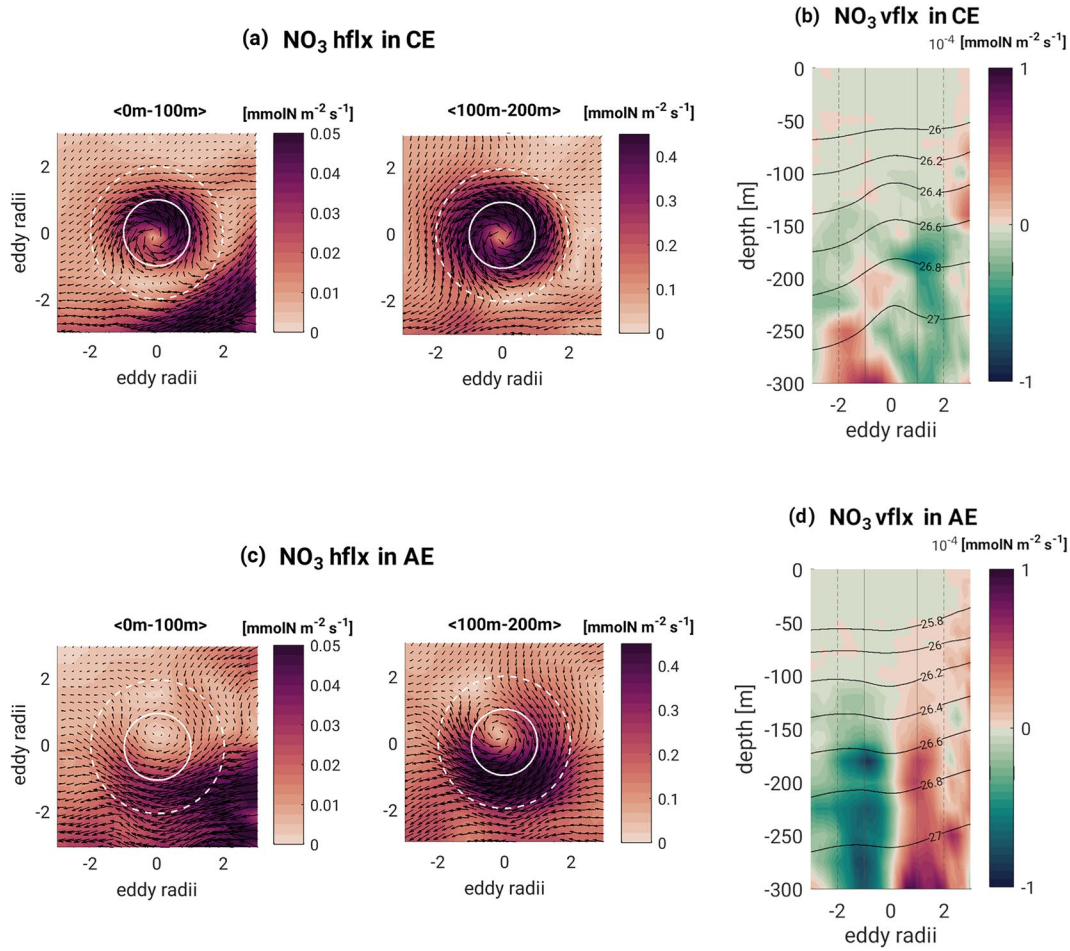

Figure 8. Advective horizontal fluxes (hflx) and advective vertical fluxes (vflx) of NO_3: (a) CE hflx, (b) CE vflx, (c) AE hflx, (d) AE vflx. Horizontal fluxes are averaged in two ranges of depth: [0 m, 100 m] and [100 m, 200 m]. Plots of hflx show the absolute magnitude of the flux overlaid by the relative vector field. Note that the range of the colorbars of hflx changes between euphotic layer and below. Vflx plots are west-east centered transects with positive values indicating upward transports and black contour lines indicating isopycnals [kg m^{-3}]. All plots refer to the first 2-day mean of month 6 of the eddy lives.

in a pattern that is either unrelated to the NO_3 anomaly (CE) or it even acts against it (AE). In fact, the dipolar pattern of the vertical velocities together with the distribution of NO_3 (Figures 4b and 4e) lead in both types of eddies to a dominantly negative vertical advective flux, especially near-surface. Not even the vertical mixing flux can explain the deep reach of the NO_3 anomalies. In fact, although mixing always acts against tracer gradients and therefore contributes positively to the nitrate influx into the low-nutrient euphotic layer, its intensity declines quickly below the MLD, reaching zero at about 200 m depth.

Therefore, deep-reaching NO_3 positive anomalies in the eddies are not explained by continuous vertical fluxes throughout the life of the eddy but either by the initial priming of the eddy core with NO_3 rich upwelled waters in CEs or by the deep influence of the eddy rotation. The latter is especially important for AEs, which smooth by stirring the sharp regional boundary of the Cape Verde front, laterally redistributing nitrate from nutrient-rich deep waters of the southern latitudes to the north. While working against this steep lateral nitrate gradient, AEs also capture precious nutrients for NP at depth around at their rim, which may eventually find their way into the euphotic layer via vertical fluxes.

3.5. Inorganic and Organic Nitrogen Fluxes Throughout the Life of the Eddies: A Story of Continuous Biological Transformations

Building on the detailed analysis of the spatial patterns of biological tracers and their fluxes in the eddies, we now discuss the temporal evolution of the eddy budgets and fluxes DIN and PON. This allows us to quantify the relative role of each process sustaining the delivery of DIN and production of PON to the euphotic layer of CEs and AEs throughout the entire lifespan of the mean tracks. Processes that affect DIN and PON inside eddies are biological uptake and release, sinking of particles, vertical mixing, and lateral and vertical transports (see Methods section). Given the differences between the spatial patterns of tracers in CEs and AEs, we separately discuss the euphotic layer fluxes and concentrations for the eddy core (0R–1R range) and for the eddy periphery (1R–2R range), respectively first for CEs and then for AEs.

3.5.1. Eddy Core Budgets

Our eddy-core budget analysis for CEs confirms their remarkable lateral isolation after the first few months of their life (Figures 9a and 9b). However, despite this lateral isolation, the initially very high DIN and PON contents of the eddies progressively decrease with time (Figures 9a and 9b, lower panels). The processes underlying this decrease are more complex than simply the loss of PON through sinking. In fact, fixed nitrogen is rapidly turned over inside the eddies, and the net balance is the result of both gains and losses.

The largest driver of the DIN depletion, especially for young CEs, is NCP, that is, the net biological production of PON. While young CEs fuel most of their NCP from initially trapped DIN, the replenishment of DIN by vertical mixing within the cores becomes increasingly relevant as the eddies age. Initially, vertical mixing supplies about 25% of the NCP, but this fraction increases to 100% for CEs older than 9 months. In our model, this vertical mixing represents the net effect of unresolved sub-grid scale processes such as small scale convection and turbulence, highlighting the role of these processes for the sustenance of production in the eddies. Yet, the substantial vertical input by vertical mixing throughout the eddy lifetime does not fully compensate for the total losses of DIN, resulting in its progressive decline over time.

Vertical advection adds to the loss of DIN from CE (Figure 9a). This is in contrast with the common illustration of vertical advection constituting a source of DIN through a radially symmetric “pumping” of nutrients in the CE's core (McGillicuddy, 2016). Two factors contribute to this result. On the one side, the dipole pattern of vertical velocities in the eddy core shows a dominance of negative (downward) advection where tracer concentrations are highest (Figures 4 and 7). On the other side, the large scale negative signature of the wind stress curl in the CanUS leads to a downward Ekman pumping (Pelegrí & Benazzouz, 2015). This large scale downwelling flux is especially important in CEs, which tend to drift northwards (Figure 2) toward the areas with the most negative wind stress curl (Bonino et al., 2021).

Despite the continued production of PON from initially trapped DIN and upward mixing of DIN, PON concentrations decrease through the CE lifetime. That is, the production of PON via NCP as the main source of PON is insufficient to compensate for the losses of PON (Figure 9b). In fact, most of PON is lost through sinking below 100 m. Advection and mixing also have a negative yet very small contribution to the decrease of PON.

In summary, CEs are initialized with remarkable amounts of DIN and PON during their formation, primarily through the trapping of upwelled waters near the coast. After this initial phase, NPP within the CE cores is sustained in large part (about 78%, according to our model) through ammonia (RP) generated by the local recycling of organic matter. NP of PON through the uptake of nitrate trapped at formation and input vertically, contributes with an additional 22% of NPP to the large PON availability of CE cores. This result highlights the importance of the CE contribution to the offshore transport of coastal PON and DIN, which, once trapped, have little chance to escape laterally from the CE core, while they get transformed by local biological activity.

Compared to CE cores, AE cores are characterized by smaller tracer fluxes and concentrations (Figures 9c and 9d) and by a slightly higher contribution of RP to total production (about 81%). In the first month of the eddy life, DIN and PON in the core of AEs are, respectively, about three to five times smaller than those of CEs. While these concentrations also decrease in the AE as they age and propagate offshore, these declines are weaker

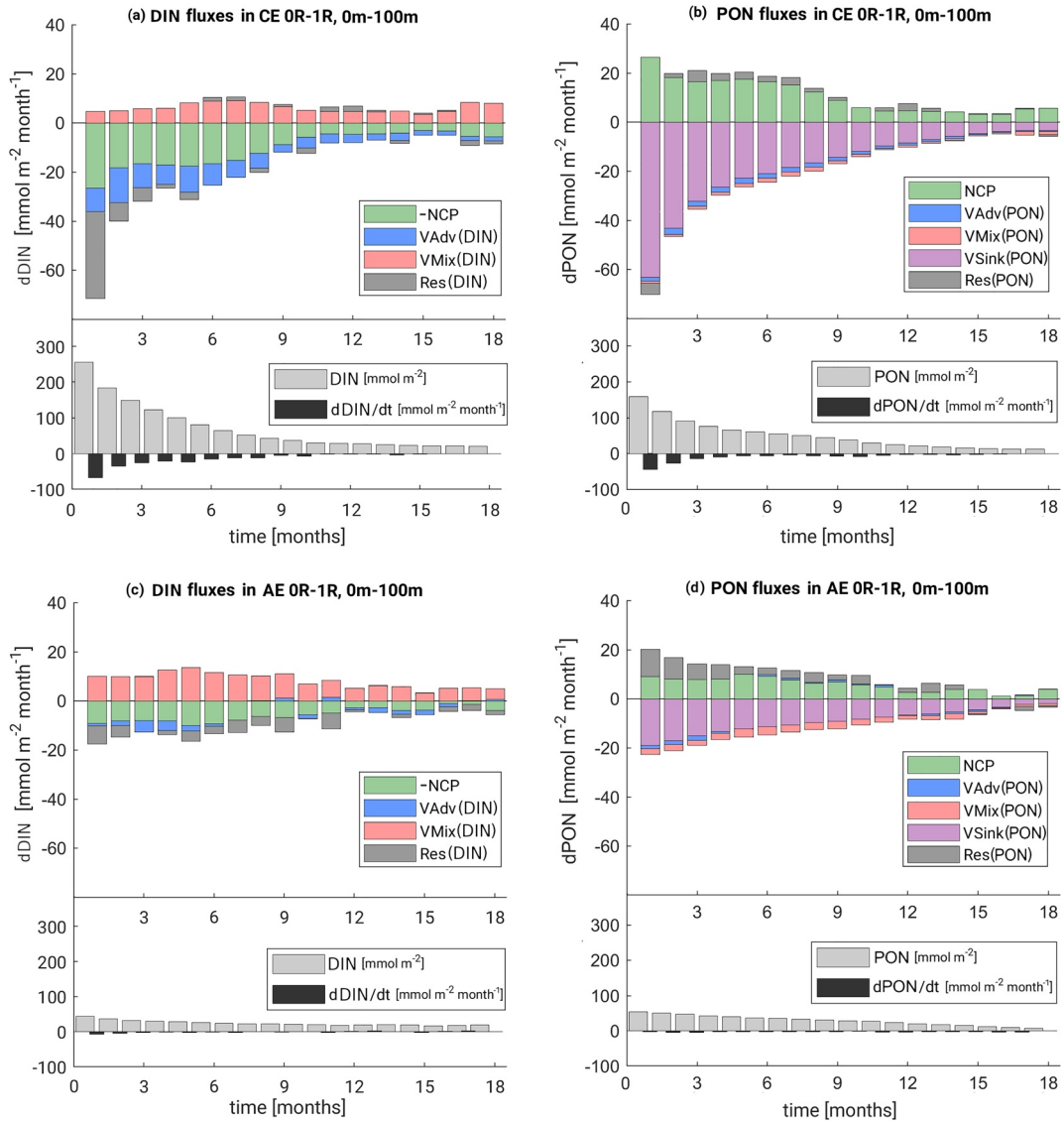

Figure 9. Fluxes of DIN and PON in the euphotic layer (0–100 m) within the eddy core (0R–1R) over the eddy life-time. (a) Upper plot: CE total monthly average DIN flux components; Lower plot: DIN monthly average concentration and tendency dDIN/dt. (b) Upper plot: CE total monthly average PON flux components; Lower plot: PON monthly average concentration and tendency dPON/dt. For each tracer, residuals are calculated as the difference between tracer tendency and the sum of all the flux components output by the model (NCP and vertical fluxes); (c) same as (a) for AE; (d) same as (b) for AE.

compared to the losses seen in CEs. The same holds for the fluxes of DIN and PON, which are also weakening more slowly in the AE cores.

In the case of the vertical advective fluxes, their smaller absolute magnitude in the core of AEs is largely due to the depletion of DIN in the euphotic zone of AEs. This is possibly partially associated with a southward drift of the AE (Figure 2) towards regions of less negative wind stress curl (Bonino et al., 2021). In fact, the net contribution of vertical advection in AE cores is not negative at all times, showing a substantially more noisy and vacillating contribution to the budget at most stages of the eddy life, compared to CEs. The vertical mixing flux in the core of AEs is larger than that in the core of CEs for both DIN and PON. This is likely due to deeper mixed layer depths (MLD) in AEs, which, combined with higher DIN concentrations at depth, results in enhanced vertical mixing (Dufois et al., 2016; Gaube et al., 2019).

The residual fluxes, consisting of lateral leakage and entrainment, are generally smaller than the main sources and sinks of DIN and PON in AE cores, although their values oscillate in time. Interestingly, these residual fluxes

are overall larger in the AE cores compared to CEs despite the lower tracer concentrations, which also results in a comparatively larger impact on the budgets. This is consistent with the lesser degree of lateral isolation of the AE cores, leading to a stronger lateral exchange at their boundaries (Figure 8).

3.5.2. Eddy Rim Budgets

The budget analyses at the eddy rim permit to shed some light into the processes driving the formation and maintenance of the peripheral tracer dipole in the euphotic layer of both CEs and AEs (Figure 10). Major differences between the CE core and rim fluxes are found in the role of the vertical advective fluxes of DIN, that are positive at the eddy rim in the first few months of its life. This is driven primarily by positive (upward) anomalies in the dipole-shaped vertical velocities at the periphery of young CEs, possibly due to the initial eddy intensification

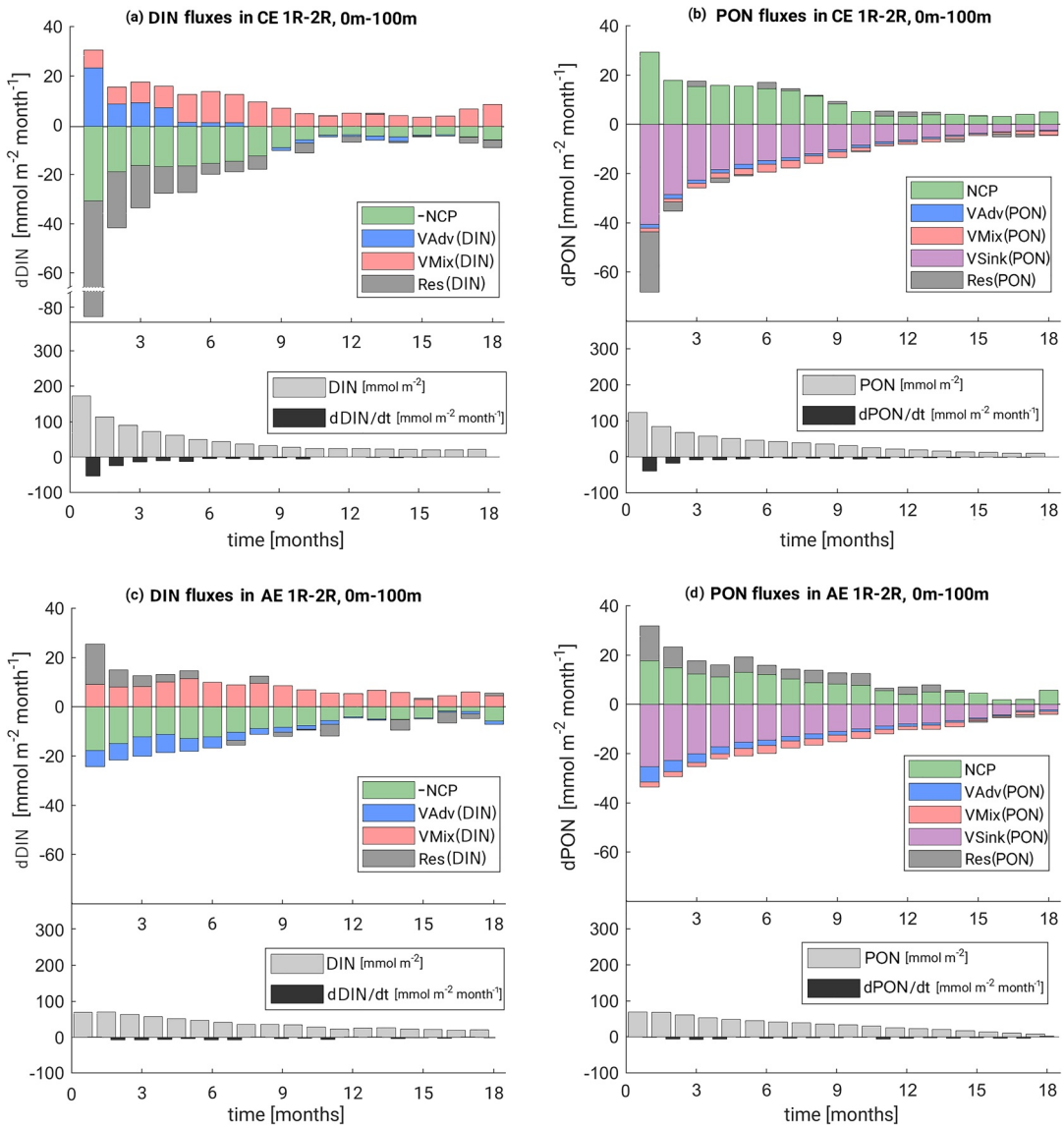

Figure 10. 1R–2R eddy budgets for DIN and PON in the euphotic layer (100 m). (a) Upper plot: CE total monthly average DIN flux components; Lower plot: DIN monthly average concentration and tendency dDIN/dt. (b) Upper plot: CE total monthly average PON flux components; Lower plot: PON monthly average concentration and tendency dPON/dt. For each tracer, residuals are calculated as the difference between tracer tendency and the sum of all the flux components output by the model (NCP and vertical fluxes); (c) same as (a) for AE; (d) same as (b) for AE.

and coupling to the upwelling front. Past the fourth month of their life, however, DIN input at the CE rim is mostly driven by mixing.

Residual DIN fluxes are also substantially larger at the CE periphery compared to the CE core, indicating that, in these eddies, the 2R perimeter is not as laterally isolated from the surrounding tracer fields as the core. This is likely due to the decrease in the rotational speed moving away from the 1R CE perimeter (Figure 3). Trends in the remaining CE periphery fluxes, especially for PON are particularly close to those observed in the CE core, with the large majority of the DIN vertical influx being supported by vertical mixing, especially after the 5th month of the CE's life (Figure 10b).

For AEs, the biological and vertical fluxes in the rim DIN budget (Figure 10c) have the same signs as those pertaining to the AE core. However, the lateral input of DIN at the rim of AEs is substantial only in the first five months of the eddy's life, when it is still relatively close to the nutrient-rich upwelling region and the eddy wraps upwelling water around its core. Successively, vertical mixing of deep nutrients into the euphotic layer is the main source of DIN at the AE rim.

In contrast to the DIN budget, the AE rim PON budget (Figure 10d) is characterized by a persistent lateral input of PON from the surrounding environment, primarily due to the high PON background concentration in the offshore euphotic layer especially at the boundary of the Cape Verde front, along which many AE tracks run (Figures 2a and 2c). The higher abundance of PON surrounding AEs compared to CEs is visible in the composite plots of the vertically integrated organic material (Figure 5). In agreement with the slope of the Cape Verde front, higher PON values are concentrated at the south-eastern boundary of the eddy. In other words, analogously to how AEs build the nutrient anomaly at depth, stirring the deep gradient in NO_3 at the Cape Verde front, they also stir the high PON concentration of the southern CanUS waters in the euphotic layer, and this way entrain additional PON at their periphery at every stage of their life.

3.5.3. Eddy Budgets Summary

In summary, average tracer fluxes in the euphotic layer of fully developed eddies (Figure 11) show that vertical mixing is the key source of new DIN from below in both CEs and AEs without major distinctions between eddy core and rim, while vertical advective fluxes mostly oppose the upward mixing of deep nutrients. In addition to the supply of new DIN from vertical mixing, CE and AE cores are primed with very different levels of DIN at their formation, resulting in a different relative importance of vertical mixing for the DIN stock in the eddy cores: while average mixing fluxes in AE cores add ∼40% to the DIN stock each month, taking ∼2.5 months to supply as much DIN as the available stock, in CE cores this number only reaches ∼12%, taking ∼8 months to replenish the local DIN stock. This further highlights the dominant role of the initial tracer trapping in CE. At the eddy rim, mixing fluxes add to both CEs and AEs about ∼20% to the local DIN stock each month.

Lateral fluxes at the CE core boundary are smaller than in AEs, indicating a better lateral isolation of the first type of eddies from the surrounding environment. In particular, monthly mean lateral fluxes at the edge of CE cores represent on average less than 0.2% of the DIN core concentration and 3.6% of the PON core concentration, while for AEs these numbers rise to 5% and 8.8%. In both types of eddies sinking fluxes dominate the loss of PON from the euphotic layer in both core and rim.

The turnover of PON and DIN through production and remineralization is intense, with both biological fluxes exceeding by far any physical flux while also having rather similar magnitudes, therefore resulting in a much smaller value of NCP. This highlights once more the importance of PON recycling in both cores and rims of the eddies, with RP representing about 3/4 of the total production at the rim of both eddy types and, respectively, 78% and 81% of the total production in the CE and AE cores (see Appendix Figure A5a). We find that biogeochemical cycling (total production and remineralization) within the eddies are more intense in the core for CEs and in the rim for AEs. Our numbers suggest that it takes about 1.5 months to rejuvenate the available PON pool in the CE core and rim and AE rim, while AE cores feature a slightly longer rejuvenation time scale of 1.7 months. in eddies in eddiesIn our analysis, the average long-living CE track lasts 14 months, while the average AE track lasts 10 months, with many tracks persisting well beyond 18 months (see Appendix: Figure A2a). This implies that the coastal organic material trapped at formation inside long-living eddies, as well as the PON generated

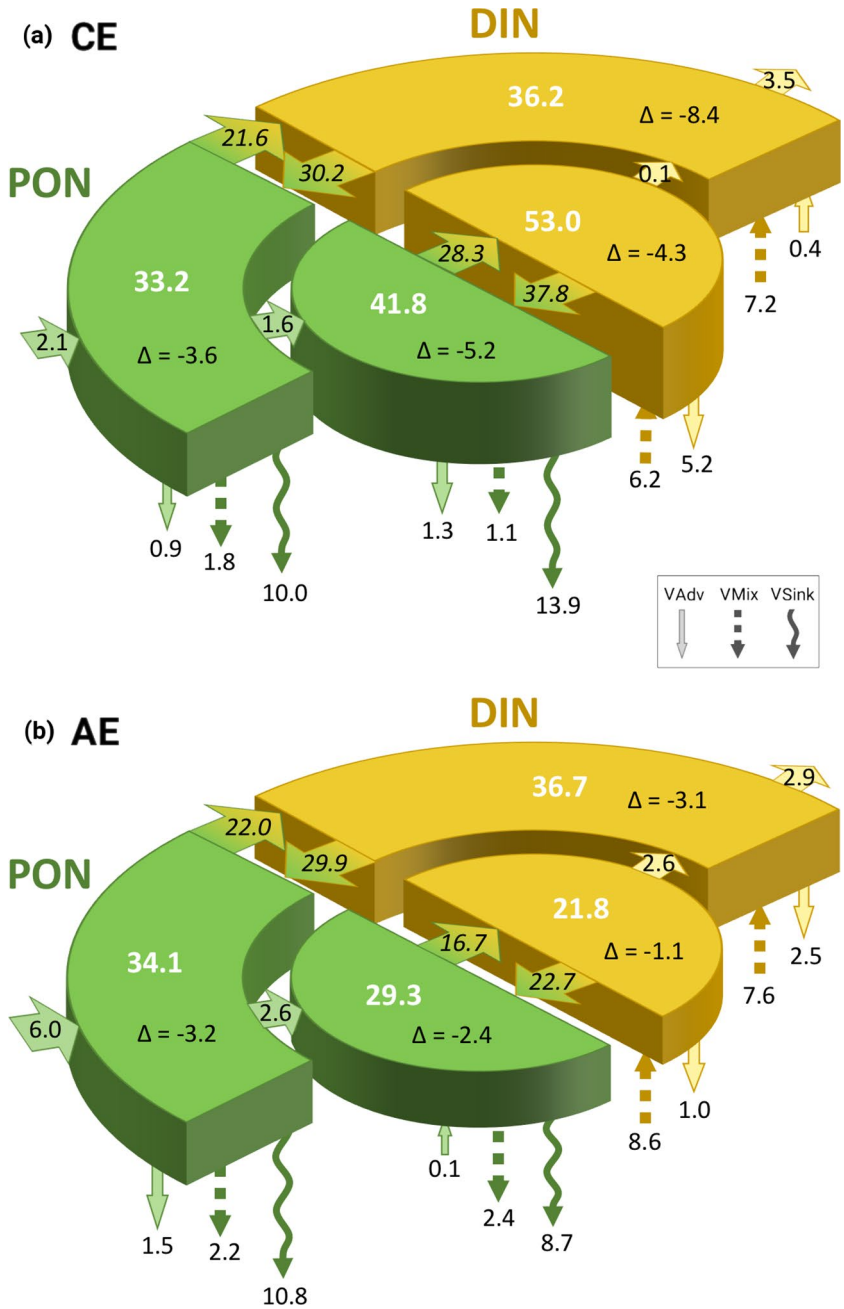

Figure 11. Budgets of PON (green) and DIN (yellow) in the euphotic layer of fully developed eddies, that is, averaged over months 4 to 15 of the eddy life. Central compartments represent the eddy core (0R–1R), outer compartments represent the eddy 1R–2R region. The thickness of each compartment is roughly proportional to the concentration of PON and DIN [mmolN m^{-2}], indicated in bold white. On each compartment, Δ represents the average time tendency of the tracer, that is, its net monthly mean variation. Vertical arrows represent physical fluxes (see legend). Horizontal arrows between compartments of the same tracer represent lateral fluxes (residuals). The lateral flux at 2R is calculated as the difference between the 1R–2R residual and the residual at 1R. Horizontal arrows that go from DIN to PON compartments represent total production, while arrows in the opposite direction represent remineralization. Tendencies and fluxes are expressed in [mmolN m^{-2} $month^{-1}$]. Sizes of arrows are only indicative of the relative intensity of the fluxes. The direction of the arrows indicates whether a flux is positive (influx) or negative (outflux).

successively through nitrate uptake, is rejuvenated multiple times along the eddy track, before being delivered to the open oligotrophic waters.

4. Discussion

4.1. CE Drag Along, AE Stir Up Biogeochemical Tracers in the Northern CanUS

In agreement with several previous studies of eddies in the CanUS, the distribution of organic matter in the CEs and AEs is fundamentally different, with most of the organic material being concentrated in the core of CEs and at the periphery of AEs (Baltar et al., 2009; Basterretxea & Arístegui, 2000; Hernández-León et al., 2007). This difference results in great part from the dominant role of trapping in CEs and stirring in AEs. The dominance of trapping of the coastal water for CEs is confirmed by their relatively homogeneous and cold and fresh temperature and salinity signature (see Appendix: Figure A4) reflecting the trapping of upwelled waters. In contrast, AEs trap less efficiently during their formation, and the waters they do trap have not only a warmer and more salty signature but also a more variable one reflecting the distribution of open water properties of the CanUS.

The key role of trapping in shaping patterns of biogeochemical tracers in CEs generated in an EBUS region was previously highlighted by Chenillat et al. (2015), who based their conclusions on a case-study of a modeled CE in a simulation of the California Upwelling System. Our analysis, with its mean track perspective, confirms the importance of trapping for the tracer budget of the mean CE core throughout the entire span of the eddy life. Next to the initial priming with upwelled waters of CE they show a remarkable lateral isolation, likely driven by the large rotational speed of these eddies, especially compared to AEs. Thanks to this lateral isolation that allows the continuous local recycling of the PON trapped at formation, CEs substantially contribute to the lateral transport of coastal material properties for several hundreds of kilometers. This strengthens the results of previous studies, while also explaining the physical mechanism behind this striking ability of CEs to deliver organic matter to the nutrient-depleted ocean (Chenillat et al., 2016; Lovecchio et al., 2018; Yamamoto et al., 2018).

Tracer patterns in the AEs of the northern CanUS, instead, are strongly influenced by the lateral stirring of the large scale regional gradient, especially due to the southern drift of AE tracks, which approach the biophysical boundary of the Cape Verde front. This front, in fact, separates the nutrient-depleted offshore waters of the open North Atlantic Subtropical Gyre from the region of the North Atlantic Tropical circulation, characterized by the DIN rich South Atlantic Central Water and by a positive wind-stress curl fueling organic matter production also offshore (Arístegui et al., 2009; Bonino et al., 2021). Through this lateral stirring, AEs have therefore an important role in shaping the large scale DIN and PON distribution of the region, laterally coupling the subtropical and tropical regions of the CanUS located respectively north and south of the Cape Verde front.

4.2. Vertical Mixing Dominates Over "Eddy-Pumping"

Among the many processes that have been proposed to drive biophysical interactions in mesoscale eddies, the vertical eddy "pumping" hypotheses has been among to the most popular (McGillicuddy, 2016; Siegel et al., 1999). In this hypothesis, the vertical excursions of isopycnals within eddies cause an effective pumping of water and tracers up (CEs) or down (AEs) through a radially symmetric rectification process that has a maximum in the eddy core. It has been emphasized that this process tends to be limited to the spin-up phase of the eddies when the isopycnals are lifted up (CEs) or suppressed downward (AEs), as this brings anomalous conditions to the lower parts of the euphotic zone within the eddy's core (Gaube et al., 2014). Despite this, the core-intensified "eddy pumping" mechanism is often cited as a process shaping the eddy tracer distribution well beyond the formation phase (Dufois et al., 2016). According to our results, this process is unimportant in well-formed eddies. The model simulated vertical velocities, and therefore vertical advective fluxes in well-formed eddies, have a dipolar structure in both CEs and AEs, with maxima at the periphery of the eddies at every stage of the eddy life. Further, these advective fluxes mostly remove both DIN and PON from the euphotic layer in cores of both AEs and CEs.

The dipolar pattern of the vertical fluxes that we found is in agreement with previous high-resolution observational studies of the structure of vertical velocities in eddies, such as Barceló-Llull et al. (2017), which however focused on a mode water anticyclone. The difficulty of collecting such high-resolution data makes these in situ studies scarce if not unique, and more of such measurements would be needed for both surface-intensified CEs and AEs. Lévy (2003) used an idealized model to study the impact of mesoscale activity on tracer gradients, and showed that mechanisms of lateral transport could better explain the correlation between the doming of isopycnals and nutrient levels than vertical fluxes, as nutrient isolines do not necessarily follow isopycnal surfaces at the

mesoscale. Our results confirm that the eddy core "pumping" scheme, even though often cited, does not capture the complexity of the pattern of upward and downward fluxes of DIN and PON in both CEs and AEs.

According to our results, vertical mixing is instead responsible for most of the vertical input of DIN in the euphotic layer of the eddies. Mixing also leads to the ejection of PON from the euphotic layer. With a lateral resolution of our model of about 4.7 km in the nearshore, vertical mixing in the model parameterizes sub-grid processes including convection and submesoscale induced fluxes. Our findings are therefore in line with several studies highlighting the key role of submesoscale and ageostrophic fluxes in both the delivery of nutrients to the euphotic layer (Dufois et al., 2016; Klein & Lapeyre, 2009; Martin & Richards, 2001) and the export of the organic material (Stukel et al., 2016), confirming the key role of these small scale fluxes in mesoscale eddies.

4.3. Beyond the Northern CanUS: Extending Our Results to Other Boundary Current Systems

The physical and biogeochemical processes that sustain DIN and PON in long-living CE and AE of the northern CanUS are likely also of relevance in other regions of the world's ocean (Gaube et al., 2014; McGillicuddy, 2016). This is especially the case for the other coastal upwelling regions that are characterized by an equatorward coastal current, in particular the other three major EBUS, such as the California, Humboldt, and Benguela Upwelling Systems. We also argue that the concepts should work for eddies generated by western boundary currents, although dedicated studies should aim to verify it.

In contrast, the applicability might not be guaranteed in coastal upwelling regions that are characterized by poleward coastal currents, since the initial priming might be rather different there. One such region is the southern CanUS (<21°N), often known as the Mauritanian-Senegalese Upwelling System. Here, trapping at formation by CE and AE may result in the initial eddy budgets having the opposite sign of anomalies to the ones found in the northern CanUS, since AEs tend to entrain the upwelled nutrient-rich waters in the Mauritanian-Senegalese Upwelling System.

Further caution is needed when considering island-generated eddies, such as those constituting the Canary Eddy Corridor (Sangrà et al., 2009). Island-generated eddies, in particular CE, can have very different properties at the formation from nearshore-generated eddies as they do not necessarily interact with the upwelled water, while they may trap or stir island shelf-waters. In their study of the Canary Eddy Corridor tracks, Sangrà et al. (2009) found that nearly the entire population of these eddies lives less than 6 months (Arístegui et al., 1997), which constitutes in our analysis the minimum life-length required for a track to be considered long-living. As a consequence, the biogeochemical evolution of the eddies generated in the northern CanUS by the Canary Archipelago may require an additional dedicated study.

An Eulerian analysis of the same model run adopted in this study highlighted seasonal variations in the rates of production in the core of the eddies of the CanUS (Bonino et al., 2021). These result from a combination of factors among which large scale temporal variations in vertical fluxes of nutrients, the seasonality of upwelling and the eddy distance from the coast. Although our annual-mean analysis captures the most important processes regulating tracer budgets in the eddies, a more detailed analysis could take the seasonal variations into account. Given that different EBUS are dominated by different temporal variability (Chavez & Messié, 2009), we expect eddy fluxes to be modulated on significantly different time scales in different upwelling systems, spanning from monthly to multi-decadal time scales.

4.4. Model Limitations

There are a number of model limitations that we need to be aware of when putting our results into perspective. This includes (a) the neglect of the interaction between the oceanic mesoscale circulation field and the wind, (b) the lack of consideration of the submesoscale, and (c) the simplicity of the oceanic biogeochemistry/ecological model.

The lack of the consideration of the interaction between wind and surface ocean circulation in the eddies is expected to result in a missing core-centered upwelling and downwelling of water masses and tracers in AE and CE, respectively (Gaube et al., 2015; Seo et al., 2016). In addition to opposing the classical "eddy pumping" flux in sign, this eddy-wind interaction process may be relevant at any stage of the eddy life, provided the presence of sufficient wind stress. In order to consider the potential error connected to the neglect of this eddy-wind

interaction term, we evaluate the vertical speeds that could be induced by the wind feedback in our region. Mean wind speeds in the northern CanUS are in the range of 6 m s^{-1}, with positive and negative oscillations that result in high peaks of about 10 m s^{-1} in the nearshore during upwelling conditions (summer; Pelegrí & Benazzouz, 2015). This wind may result in vertical upward and downward Ekman pumping velocities of a few cm per day, respectively in AE and CE (Chelton, 2013). Compared to our modeled eddy vertical velocities, of the order of 0.1–0.6 m day^{-1} (Figure 4), this Ekman upwelling is small but not completely negligible.

In the case of CE, the eddy/wind interaction may result in an increase of the vertical advective export of organic material at depth and a decrease of the nutrient supply from below, therefore consuming faster the trapped PON and DIN reservoir, and limiting NP. This would mostly affect the time derivative of the PON and DIN concentration, without affecting the main result of CE as highly productive trapping eddies with a tracer-rich core. For AE, this core-centric Ekman upwelling may stimulate higher levels of (new) production in the eddy center; while this may slightly change the radial distribution of the PON concentration, it is unlikely to affect the importance of the stirring and mixing. Given the strong negative anomaly in the AE cores, the wind feedback is also not expected to be able to result in a PON maximum in the eddy core, but may potentially flatten the radial gradient.

The lack of consideration of the oceanic submesoscale impacts primarily our conclusion about the processes that govern the vertical mixing and that are so crucial in supplying nutrients to the eddies after the initial phase. As we do not explicitly resolve the submesoscale dynamics, we would expect that in a higher resolution model the contribution of such vertical fluxes would be even more important (Mahadevan, 2016; Zhong & Bracco, 2013; Zhong et al., 2017). Submesoscale processes could also alter the trapping efficiency, given that frontal instabilities could occur at the boundaries of the eddies, thereby shortening also the life time of eddies via dissipation (Lévy et al., 2012). However, as this effect is expected to affect CEs and AEs equally, relative differences between the two types of eddies are likely to be maintained.

We expect that the simplicity of the employed biogeochemical and ecological model has relatively minor impact on the conclusions. The processes driving the eddy responses tend to primarily of physical nature, rendering the details of how the supplied nitrogen is being transformed within the marine food-web less important. An important exception is the lack of consideration of dissolved organic nitrogen (DON), but as already demonstrated and discussed by Lovecchio et al. (2018, 2017), our fully considered small detrital pool resembles in many ways the DON pool. Since particulate matter is horizontally advected in our model, this very slowly sinking pool can be horizontally transported over great distances, analogous to DON.

5. Summary and Conclusions

Using output from our high-resolution modeling study, we determined how production and export are sustained in the eddies of the northern CanUS. To this end, we analyzed the evolution of the DIN and PON stocks and fluxes inside long-living mesoscale eddies as they propagate offshore. We find substantial differences in the biogeochemical and physical characteristics between the mean CEs and AEs in the northern CanUS that persist over the course of one and a half years of eddy life time. These characteristics, and especially the spatial patterns are regulated by a different set of physical processes in CEs versus AEs.

CEs are characterized by high stocks of biogeochemical tracers in their core throughout their lifetime, with the maximum PON and DIN concentrations found at formation, when they trap the nutrient- and organic matter-rich waters characteristic of recent coastal upwelling. The cores of these eddies are efficiently laterally isolated from the surrounding environment, limiting the lateral exchange of tracers, while vertical fluxes drive the evolution of the PON and DIN budgets. Vertical mixing, rather than vertical advection, is the main source of extra DIN for the CE core. However, this vertical supply of PON and DIN is small compared to the DIN and PON that CE had trapped at formation in the coastly upwelled waters. CEs rely mostly on their initial priming with DIN and PON to sustain the production over their lifetime. The loss of fixed nitrogen by sinking leads to a progressive reduction in the stock of DIN and PON.

AE cores are poor in biogeochemical tracers, while their concentrations are elevated at the periphery of the eddies, between 1 and 2 eddy radii from the center. Also in AEs, vertical mixing contributes positively to the eddy nutrient budget both in the core and at the rim of the eddies, feeding the local production of PON. In AE cores, the vertical mixing input of DIN, favored by the local deepening of the isopycnals, is especially crucial due to the

otherwise low tracer stocks. Lateral stirring of the strong north-south large scale gradient of PON and DIN in the CanUS, combined to the slight southward drift of the AE tracks, is key in generating the tracer patterns at the rim of AEs. At depth, stirring builds a deep-reaching nitrate anomaly in AEs, while in the euphotic layer it results in significant lateral input of PON at the eddy rim.

In both types of eddies, past the first 2 months of the eddy lives, local recycling constitutes about 3/4 of the total production. Our numbers also indicate that on average the entire PON stock is rejuvenated between 7 and 8 times during each year of the eddy lives. As a consequence, the organic material that sinks to the deep ocean as well as the organic material that is released when the eddies reach the end of their lifetime is the result of intense transformations that have turned over the local PON and DIN stocks several times. This is especially important in CEs, where RP reconstitutes the abundant PON stock and promotes the lateral export of the trapped coastally derived organic matter toward the offshore waters. Future in situ observations could be aimed at studying the detailed pattern of biogeochemical transformations driving this continuous recycling as well as potential changes in the community composition within the eddies at different stages of their lives.

On the large scale, our results imply that both CEs and AEs have a key role in determining the regional tracer distribution. Thanks to a high degree of lateral isolation, CEs are efficient at delivering coastal tracers toward the oligotrophic North Atlantic Gyre, while also fueling the deep open waters with transitory bursts of sinking PON (Lovecchio et al., 2018). AEs, instead, contribute to smooth the large-scale gradients of DIN and PON, especially at the sharp Cape Verde front that separates the nutrient-rich tropical circulation from the oligotrophic North Atlantic gyre.

Additional studies should be aimed at better understanding both the drivers behind the different trapping efficiencies of AEs and CEs and the fine pattern of three-dimensional advective fluxes in the eddies. According to our results, while sub-grid (sub-mesoscale) fluxes are sources of nutrients for the eddies, vertical advective fluxes have a negative net contribution to the nutrient stocks and are characterized by a dipolar pattern with maxima at the eddy periphery. High-resolution in situ observations of these velocities are rare, however, the limited data available are in agreement with our results (Barceló-Llull et al., 2017). This should motivate future investigations targeting these velocity patterns in greater detail in both surface- and subsurface-intensified eddies.

Appendix A: Additional Figures

This Appendix contains five Figures. Figure A1 shows the Taylor diagram for the region of study, Figure A2 shows the mean number of averaged eddies and their mean offshore distance as a function of the eddy life time, Figure A3 shows the average CE and AE on the first time step of the track, Figure A4 shows the mean properties of the eddy cores across the entire ensemble of averaged CEs and AEs, and Figure A5 shows the portion of total production sustained by regenerated production in the average eddies and in the study region.

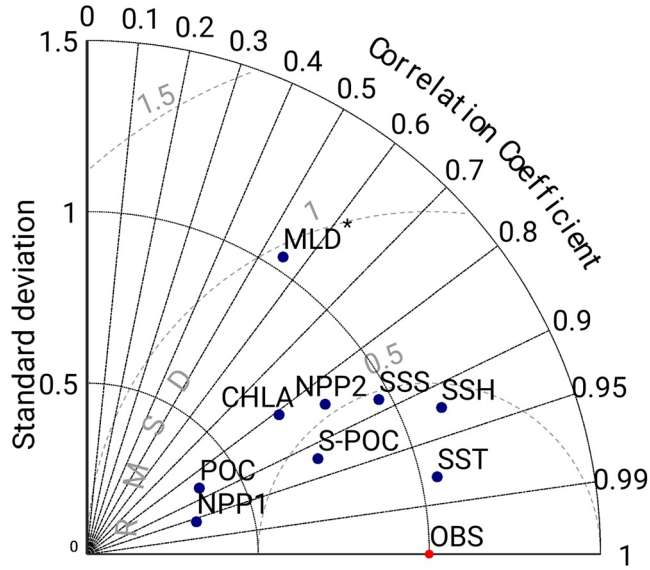

Figure A1. Annual mean Taylor diagram for the region of the CanUS spanned by the eddy tracks ([17°N, 35°N] x [5°W, 45°W]), climatological annual mean fields. Used data sets-Sea Surface Temperature (SST): AVHRR (Reynolds et al., 2007); Sea Surface Salinity (SSS): CARS (Ridgway et al., 2002); Sea Surface Height (SSH): Aviso CMDT Rio05 (Rio & Hernandez, 2004); Mixed Layer Depth (MLD): Argo DT-0.2 (Argo, 2000; Montégut et al., 2004); Chlorophyll (CHLA): SeaWiFS NASA-OBPG (2010); Net Primary Production data set 1 (NPP1): SeaWiFS VGPM (Behrenfeld & Falkowski, 1997); Net Primary Production data set 2 (NPP2): SeaWiFS CbPM (Westberry et al., 2008); Surface Particulate Organic Carbon (S-POC): SeaWiFS POC (NASA-OB.DAAC, 2010); Particulate Organic Carbon (POC): cruise POC data AMT (BODC-NERC, 2014), ANT (ANT, 2005), Geotraces (GEOTRACES, 2010). Note that MLD* = MLD/2 due to the large standard deviation (STD) that would not fit into the diagram, here plotted as half the actual STD value.

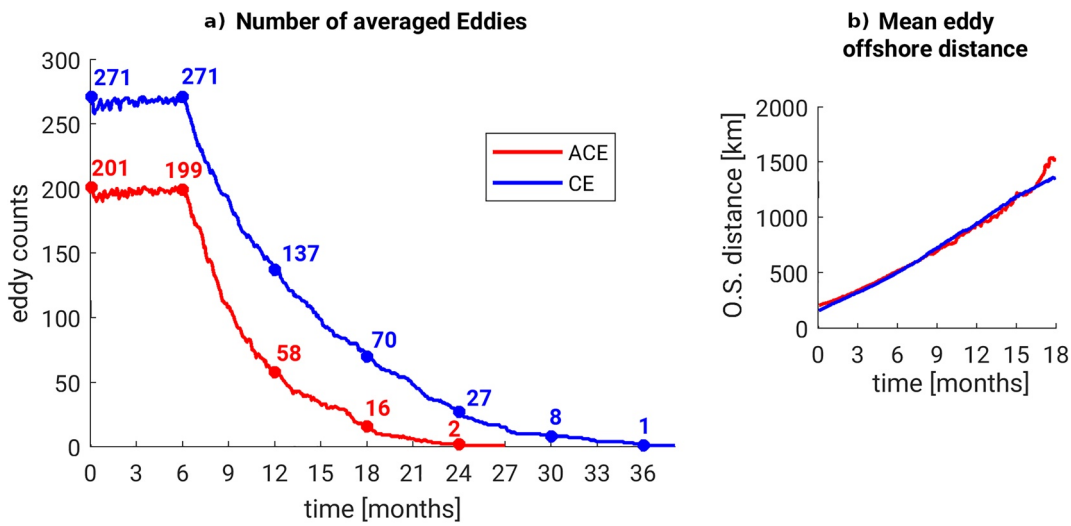

Figure A2. (a) Number of eddies averaged per day when building the track composites; oscillations result from possible non-considered "virtual eddies" created by the rejoining of broken tracks (see Methods section). (b) Mean eddy offshore distance for CEs (blue) and AEs (red) as a function of the offshore distance from the CanUS coastline.

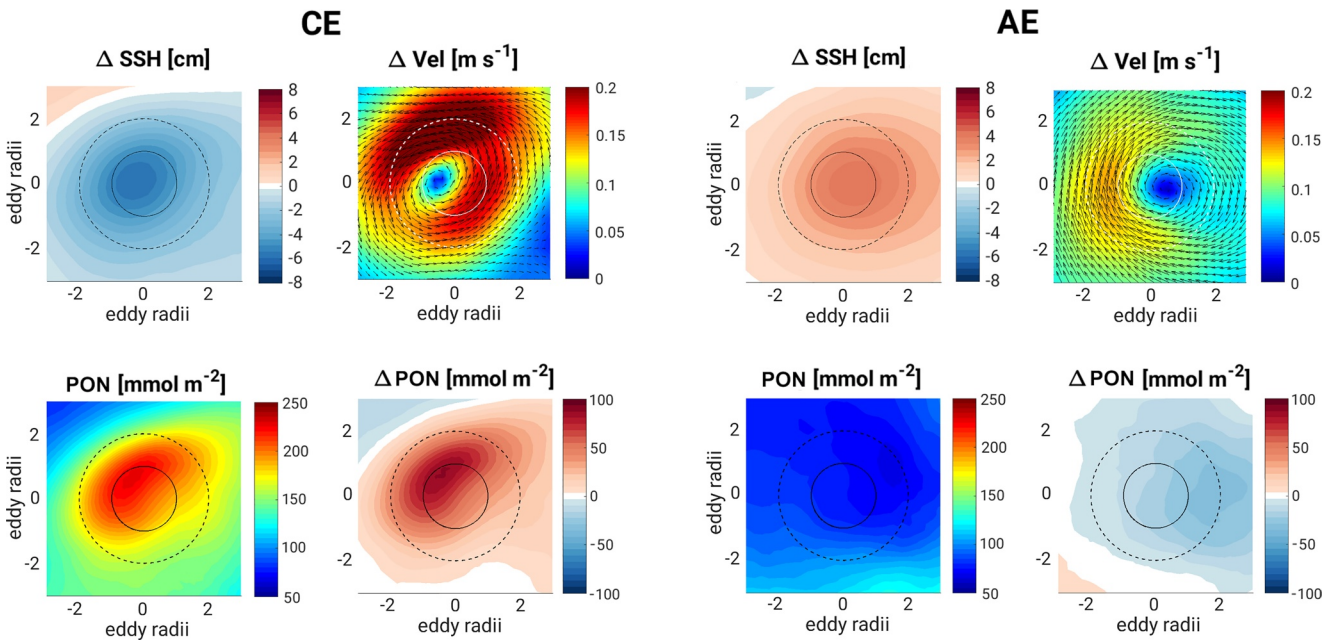

Figure A3. CE and AE physical properties and PON concentration integrated in the first 200 m at birth (first 2-day-average step of the eddy life), when the eddy is first identified by the algorithm. First row: anomaly of sea surface height (ΔSSH) and anomaly of velocities (ΔVel) respect to the reference mean fields. Second row: absolute value of $\int_{-200m}^{0}$PON dz (in the plot simply PON) and eddy anomaly Δ $\int_{-200m}^{0}$PON dz respect to the reference mean (in the plot simply ΔPON).

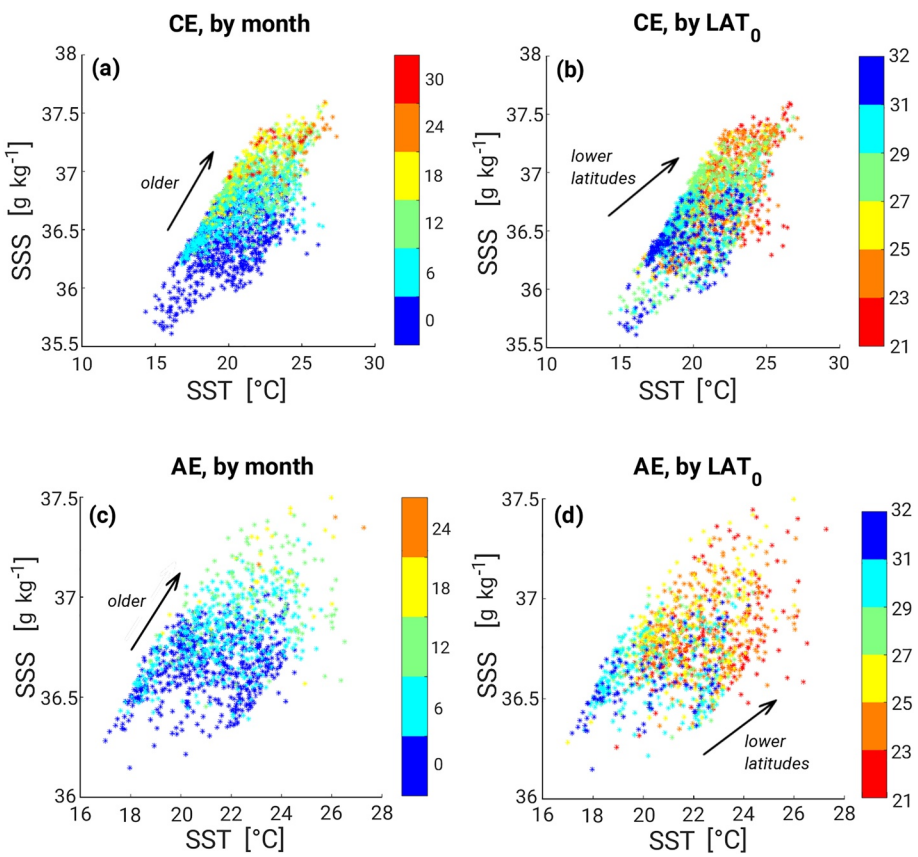

Figure A4. Mean properties of the eddy cores for each track at the moment of formation and then every 6 months. Left column: eddies are colored by their age (months from formation). Right column: eddies are colored by the latitude of formation (LAT_0) of their track. Panels description: (a and b) CEs in the space of SST and SSS; (c and d) AEs in the space of SST and SSS.

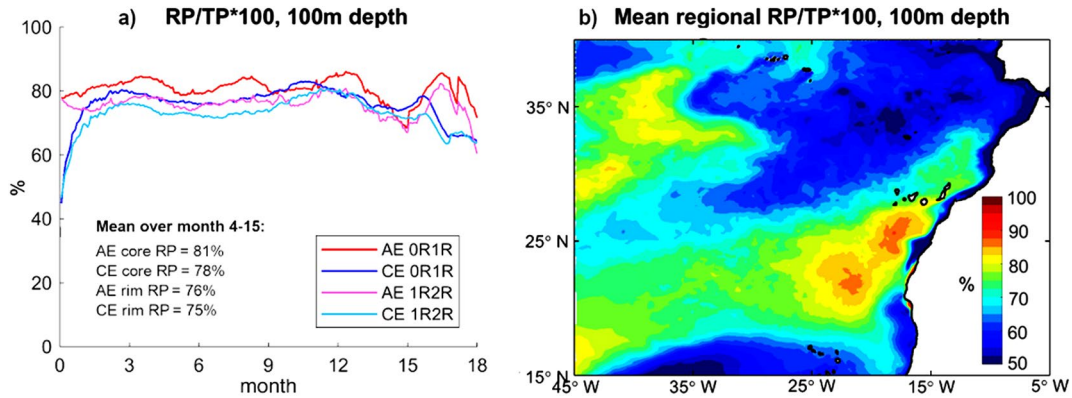

Figure A5. Percentage of total production (TP) sustained by regenerated production (RP) in the euphotic layer of: (a) the mean cyclonic and anticyclonic eddy core and rim along their lifetime; (b) the climatological mean over the 24 yr of model analysis output in the study region. Subplot (a) also indicates the mean RP contribution to TP for the core and rim of fully developed eddies, in analogy with Figure 11.

Conflict of Interest

The authors declare no conflicts of interest relevant to this study.

Data Availability Statement

The data have been registered at the ETH library archive and are available at: https://www.research-collection.ethz.ch/handle/20.500.11850/278536 (last access: December 05, 2021).

Acknowledgments
The authors would like to thank Dr. Martin Frischknecht and Dr. Cara Nissen for their insightful comments, Dr. Javier Arístegui for his suggestions and for providing his valuable opinion on the question at hand and Dr. David Byrne for his advice. The authors also thank Damian Loher for his technical support. This research was financially supported by the Swiss Federal Institute of Technology Zürich (ETH Zürich) and the Swiss National Science Foundation (Project CALNEX, grant No.149 384). The simulations were performed at the HPC cluster of ETH Zürich, Euler, which is located in the Swiss Supercomputing Center (CSCS) in Lugano and operated by ETH ITS Scientific IT Services in Zurich.

References

Abraham, E. R. (1998). The generation of plankton patchiness by turbulent stirring. *Nature*, *391*, 577–580. https://doi.org/10.1038/35361

Amores, A., Melnichenko, O., & Maximenko, N. (2017). Coherent mesoscale eddies in the North Atlantic subtropical gyre: 3-D structure and transport with application to the salinity maximum. *Journal of Geophysical Research: Oceans*, *122*(1), 23–41. https://doi.org/10.1002/2016JC012256

ANT. (2005). *Particulate Organic Carbon (POC) (Tech. Rep.)*. Retrieved from https://seabass.gsfc.nasa.gov/cruise/ant-xxiii-1

Argo. (2000). *Argo float data and metadata (Tech. Rep.)*. Global Data Assembly Centre (Argo GDAC) SEANOE. https://doi.org/10.17882/42182

Arístegui, J., Barton, E. D., Álvarez-Salgado, X. A., Santos, M. P., Figueiras, F. G., Kifani, S., & Demarq, H. (2009). Sub-regional ecosystem variability in the Canary current upwelling. *Progress in Oceanography*, *83*, 33–48. https://doi.org/10.1016/j.pocean.2009.07.031

Arístegui, J., Tett, P., Hernández-Guerra, A., Basterretxea, G., Montero, M., Wild, K., et al. (1997). The influence of island-generated eddies on chlorophyll distribution: A study of mesoscale variation around Gran Canaria. *Deep Sea Research Part I: Oceanographic Research Papers*, *44*(1), 71–96. https://doi.org/10.1016/S0967-0637(96)00093-3

Baltar, F., Arístegui, J., Montero, M. F., Espino, M., Gasol, J. M., & Herndl, G. J. (2009). Mesoscale variability modulates seasonal changes in the trophic structure of nano- and picoplankton communities across the NW Africa-Canary Islands transition zone. *Progress in Oceanography*, *83*(1), 180–188. https://doi.org/10.1016/j.pocean.2009.07.016

Barceló-Llull, B., Pallàs-Sanz, E., Sangrà, P., Martínez-Marrero, A., Estrada-Allis, S. N., & Arístegui, J. (2017). Ageostrophic secondary circulation in a subtropical intrathermocline eddy. *Journal of Physical Oceanography*, *47*(5), 1107–1123. https://doi.org/10.1175/JPO-D-16-0235.1

Barton, E., Arístegui, J., Tett, P., Cantón, M., Garcıía-Braun, J., Hernández-León, S., et al. (1998). The transition zone of the Canary current upwelling region. *Progress in Oceanography*, *41*(4), 455–504. https://doi.org/10.1016/S0079-6611(98)00023-8

Basterretxea, G., & Arístegui, J. (2000). Mesoscale variability in phytoplankton biomass distribution and photosynthetic parameters in the Canary-NW African coastal transition zone. *Marine Ecology Progress Series*, *197*, 27–40. https://doi.org/10.3354/meps197027

Behrenfeld, M. J., & Falkowski, P. G. (1997). Photosynthetic rates derived from satellite-based chlorophyll concentration. *Limnology & Oceanography*, *42*(1), 1–20. https://doi.org/10.4319/lo.1997.42.1.0001

BODC-NERC, A. (2014). *Particulate Organic carbon (POC) from Atlantic Meridional Transect (AMT) (Tech. Rep.)*. Natural Environment Research Council. Retrieved from http://www.amt-uk.org/Home

Bonino, G., Lovecchio, E., Gruber, N., Münnich, M., Masina, S., & Iovino, D. (2021). Drivers and impact of the seasonal variability of the organic carbon offshore transport in the Canary Upwelling System. *Biogeosciences*, *18*, 2429–2448. https://doi.org/10.5194/bg-18-2429-2021

Brochier, T., Mason, E., Moyano, M., Berraho, A., Colas, F., Sangrá, P., et al. (2014). Ichthyoplankton transport from the African coast to the Canary Islands. *Journal of Marine Systems*, *87*, 109–122.

Carr, M.-E. (2002). Estimation of potential productivity in the eastern boundary currents using remote sensing. *Deep Sea Research II: Topical Studies in Oceanography*, *49*(1–3), 59–80. https://doi.org/10.1016/S0967-0645(01)00094-7

Carr, M.-E., & Kearns, E. J. (2003). Production regimes in four eastern boundary current systems. *Deep Sea Research II: Topical Studies in Oceanography*, *50*(22–26), 3199–3221. https://doi.org/10.1016/j.dsr2.2003.07.015

Chaigneau, A., Eldin, G., & Dewitte, B. (2009). Eddy activity in the four major upwelling systems from satellite altimetry (1992–2007). *Progress in Oceanography*, *83*(1), 117–123. https://doi.org/10.1016/j.pocean.2009.07.012

Chaigneau, A., Le Texier, M., Eldin, G., Grados, C., & Pizarro, O. (2011). Vertical structure of mesoscale eddies in the eastern South Pacific Ocean: A composite analysis from altimetry and Argo profiling floats. *Journal of Geophysical Research: Oceans*, *116*(C11), C11025. https://doi.org/10.1029/2011JC007134

Chavez, F. P., & Messié, M. (2009). A comparison of eastern boundary upwelling ecosystems. *Progress in Oceanography*, *83*(1–4), 80–96. https://doi.org/10.1016/j.pocean.2009.07.032

Chelton, D. B. (2013). Ocean-atmosphere coupling: Mesoscale eddy effects. *Nature Geoscience*, *6*, 594–595. https://doi.org/10.1038/ngeo1906

Chelton, D. B., Gaube, P., Schlax, M. G., Early, J. J., & Samelson1, R. M. (2011). The influence of nonlinear mesoscale eddies on near-surface oceanic chlorophyll. *Science*, *334*(6054), 328–332. https://doi.org/10.1126/science.1208897

Chelton, D. B., Schlax, M. G., & Samelson, R. M. (2011). Global observations of nonlinear mesoscale eddies. *Progress in Oceanography*, *91*(2), 167–216. https://doi.org/10.1016/j.pocean.2011.01.002

Chelton, D. B., Schlax, M. G., Samelson, R. M., & de Szoeke, R. A. (2007). Global observations of large oceanic eddies. *Geophysical Research Letters*, *34*(15), L15606. https://doi.org/10.1029/2007GL030812

Chenillat, F., Franks, P. J. S., & Combes, V. (2016). Biogeochemical properties of eddies in the California current system. *Geophysical Research Letters*, *43*(11), 5812–5820. https://doi.org/10.1002/2016GL068945

Chenillat, F., Franks, P. J. S., Rivière, P., Capet, X., Grima, N., & Blanke, B. (2015). Plankton dynamics in a cyclonic eddy in the southern California current system. *Journal of Geophysical Research: Oceans*, *120*(8), 5566–5588. https://doi.org/10.1002/2015JC010826

Dee, D. P., Uppala, S. M., Simmons, A. J., Berrisford, P. P. P., Kobayashi, S., Andrae, U., et al. (2011). The Era-Interim reanalysis: Configuration and performance of the data assimilation system. *Quarterly Journal of the Royal Meteorolgical Society*, *137*(656), 553–597. https://doi.org/10.1002/qj.828

d'Ovidio, F., Monte, S. D., Penna, A. D., Cotté, C., & Guinet, C. (2013). Ecological implications of eddy retention in the open ocean: A Lagrangian approach. *Journal of Physics A: Mathematical and Theoretical*, *46*(25), 254023. http://stacks.iop.org/1751-8121/46/i=25/a=254023

Dufois, F., Hardman-Mountford, N. J., Greenwood, J., Richardson, A. J., Feng, M., & Matear, R. J. (2016). Anticyclonic eddies are more productive than cyclonic eddies in subtropical gyres because of winter mixing. *Science Advances*, *2*(5), e1600282. https://doi.org/10.1126/sciadv.1600282

Everett, J. D., Macdonald, H., Baird, M. E., Humphries, J., Roughan, M., & Suthers, I. M. (2015). Cyclonic entrainment of preconditioned shelf waters into a frontal eddy. *Journal of Geophysical Research: Oceans*, *120*(2), 677–691. https://doi.org/10.1002/2014JC010301

Faghmous, J. H., Frenger, I., Yao, Y., Warmka, R., Lindell, A., & Kumar, V. (2015). A daily global mesoscale ocean eddy data set from satellite altimetry. *Scientific Data*, *2*. https://doi.org/10.1038/sdata.2015.28

Falkowski, P. G., Ziemann, D., Kolber, Z., & Bienfang, P. K. (1991). Role of eddy pumping in enhancing primary production in the ocean. *Nature*, *352*(6330), 55. https://doi.org/10.1038/352055a0

Frenger, I., Münnich, M., & Gruber, N. (2018). Imprint of southern ocean mesoscale eddies on chlorophyll. *Biogeosciences*, *15*(15), 4781–4798. https://doi.org/10.5194/bg-15-4781-2018

Frenger, I., Münnich, M., Gruber, N., & Knutti, R. (2015). Southern ocean eddy phenomenology. *Journal of Geophysical Research: Oceans*, *120*(11), 7413–7449. https://doi.org/10.1002/2015JC011047

Fu, L.-L., Chelton, D. B., Traon, P.-Y. L., & Morrow, R. (2010). Eddy dynamics from satellite altimetry. *Oceanography*, *23*. https://doi.org/10.5670/oceanog.2010.02

Gaube, P., Chelton, D. B., Samelson, R. M., Schlax, M. G., & O'Neill, L. W. (2015). Satellite observations of mesoscale eddy-induced Ekman pumping. *Journal of Physical Oceanography*, *45*(1), 104–132. https://doi.org/10.1175/JPO-D-14-0032.1

Gaube, P., McGillicuddy, D. J., Chelton, D. B., Behrenfeld, M. J., & Strutton, P. G. (2014). Regional variations in the influence of mesoscale eddies on near-surface chlorophyll. *Journal of Geophysical Research: Oceans*, *119*(12), 8195–8220. https://doi.org/10.1002/2014JC010111

Gaube, P., McGillicuddy, J. D., Jr, & Moulin, A. J. (2019). Mesoscale eddies modulate mixed layer depth globally. *Geophysical Research Letters*, *46*(3), 1505–1512. https://doi.org/10.1029/2018gl080006

GEOTRACES. (2010). *Particulate Organic Carbon (POC) (Tech. Rep.)*. Retrieved from http://www.bodc.ac.uk/geotraces/

Gruber, N., Frenzel, H., Doney, S. C., Marchesiello, P., McWilliams, J. C., Oram, J. R., et al. (2006). Eddy-resolving simulation of plankton ecosystem dynamics in the California current system. *Deep Sea Research I: Oceanographic Research Papers*, *53*(9), 1483–1516. https://doi.org/10.1016/j.dsr.2006.06.005

Gruber, N., Lachkar, Z., Frenzel, H., Marchesiello, P., Münnich, M., McWilliams, J. C., et al. (2011). Eddy-induced reduction of biological production in eastern boundary upwelling systems. *Nature Geoscience*, *4*, 787–792. https://doi.org/10.1038/ngeo1273

Hernández-León, Rodríguez, J., Moyano, M., & Arı′stegui, J. (2007). The coastal-ocean transition zone in the Canary current system. *Globec International Newsletter*, 26–28. Retrieved from https://acceda.ulpgc.es:8443/bitstream/10553/273/1/5138.pdf

Ito, T., & Marshall, J. (2008). Control of lower-limb overturning circulation in the southern ocean by diapycnal mixing and mesoscale eddy transfer. *Journal of Physical Oceanography*, *38*(12), 2832–2845. https://doi.org/10.1175/2008jpo3878.1

José, Y. S., Aumont, O., Machu, E., Penven, P., Moloney, C., & Maury, O. (2014). Influence of mesoscale eddies on biological production in the Mozambique channel: Several contrasted examples from a coupled ocean-biogeochemistry model. *Deep Sea Research Part II: Topical Studies in Oceanography*, *100*(Supplement C), 79–93. https://doi.org/10.1016/j.dsr2.2013.10.018

José, Y. S., Dietze, H., & Oschlies, A. (2017). Linking diverse nutrient patterns to different water masses within anticyclonic eddies in the upwelling system off Peru. *Biogeosciences*, *14*(6), 1349–1364. https://doi.org/10.5194/bg-14-1349-2017

José, Y. S., Penven, P., Aumont, O., Machu, E., Moloney, C., Shillington, F., et al. (2016). Suppressing and enhancing effects of mesoscale dynamics on biological production in the Mozambique channel. *Journal of Marine Systems*, *158*(Supplement C), 129–139. https://doi.org/10.1016/j.jmarsys.2016.02.003

Karstensen, J., Fiedler, B., Schütte, F., Brandt, P., Körtzinger, A., Fischer, G., et al. (2015). Open ocean dead zones in the tropical North Atlantic Ocean. *Biogeosciences*, *12*(8), 2597–2605. https://doi.org/10.5194/bg-12-2597-2015

Karstensen, J., Schütte, F., Pietri, A., Krahmann, G., Fiedler, B., Grundle, D., et al. (2017). Upwelling and isolation in oxygen-depleted anticyclonic mode water eddies and implications for nitrate cycling. *Biogeosciences*, *14*(8), 2167–2181. https://doi.org/10.5194/bg-14-2167-2017

Klein, P., & Lapeyre, G. (2009). The oceanic vertical pump induced by mesoscale and submesoscale turbulence. *Annual Review of Marine Science*, *1*(1), 351–375. https://doi.org/10.1146/annurev.marine.010908.163704

Klocker, A., & Abernathey, R. (2014). Global patterns of mesoscale eddy properties and diffusivities. *Journal of Physical Oceanography*, *44*(3), 1030–1046. https://doi.org/10.1175/JPO-D-13-0159.1

Koszalka, I., Ceballos, L., & Bracco, A. (2010). Vertical mixing and coherent anticyclones in the ocean: The role of stratification. *Nonlinear Processes in Geophysics*, *17*(1), 37–47. https://doi.org/10.5194/npg-17-37-2010

Lachkar, Z., & Gruber, N. (2011). What controls biological production in coastal upwelling systems? Insights from a comparative modeling study. *Biogeosciences*, *8*, 2961–2976. https://doi.org/10.5194/bg-8-2961-2011

Lachkar, Z., Smith, S., Lévy, M., & Pauluis, O. (2016). Eddies reduce denitrification and compress habitats in the Arabian Sea. *Geophysical Research Letters*, *43*(17), 9148–9156. https://doi.org/10.1002/2016GL069876

Laiolo, L., McInnes, A. S., Matear, R., & Doblin, M. A. (2016). Key drivers of seasonal plankton dynamics in cyclonic and anticyclonic eddies off east Australia. *Frontiers in Marine Science*, *3*, 155. https://doi.org/10.3389/fmars.2016.00155

Lévy, M. (2003). Mesoscale variability of phytoplankton and of new production: Impact of the large scale nutrient distribution. *Journal of Geophysical Research: Oceans*, *108*(C11). https://doi.org/10.1029/2002jc001577

Lévy, M., Ferrari, R., Franks, P. J. S., Martin, A. P., & Rivière, P. (2012). Bringing physics to life at the submesoscale. *Geophysical Research Letters*, *39*(14). https://doi.org/10.1029/2012gl052756

Liu, F., Tang, S., Huang, R. X., & Yin, K. (2017). The asymmetric distribution of phytoplankton in anticyclonic eddies in the western south China Sea. *Deep Sea Research Part I: Oceanographic Research Papers*, *120*(Supplement C), 29–38. https://doi.org/10.1016/j.dsr.2016.12.010

Lovecchio, E., Gruber, N., & Münnich, M. (2018). Mesoscale contribution to the long-range offshore transport of organic carbon from the Canary Upwelling System to the open North Atlantic. *Biogeosciences*, *15*(16), 5061–5091. https://doi.org/10.5194/bg-15-5061-2018

Lovecchio, E., Gruber, N., Münnich, M., & Lachkar, Z. (2017). On the long-range offshore transport of organic carbon from the Canary Upwelling System to the open North Atlantic. *Biogeosciences*, *14*(13), 3337–3369. https://doi.org/10.5194/bg-14-3337-2017

Mackas, D. L., Strub, P. T., Thomas, A., & Montecino, V. (2006). Eastern ocean boundaries, pan-regional overview. In A. R. Robinson & K. Brink (Eds.), *The Sea, volume 14: The global coastal ocean (chap. 2)*. Harvard University Press.

Mahadevan, A. (2014). Eddy effects on biogeochemistry. *Nature*, *506*, 168–169. https://doi.org/10.1038/nature13048

Mahadevan, A. (2016). The impact of submesoscale physics on primary productivity of plankton. *Annual Review of Marine Science*, *8*(1), 161–184. https://doi.org/10.1146/annurev-marine-010814-015912

Mahadevan, A., & Campbell, J. W. (2002). Biogeochemical patchiness at the sea surface. *Geophysical Research Letters*, *29*(19), 32-1–32-4. https://doi.org/10.1029/2001GL014116

Mahadevan, A., Thomas, L. N., & Tandon, A. (2008). Comment on "eddy/wind interactions stimulate extraordinary mid-ocean plankton blooms". *Science*, *320*(5875), 448. https://doi.org/10.1126/science.1152111

Marchesiello, P., McWilliams, J. C., & Shchepetkin, A. (2003). Equilibrium structure and dynamics of the California current system. *Journal of Physical Oceanography*, *33*(4), 753–783. https://doi.org/10.1175/1520-0485(2003)33<753:esadot>2.0.co;2

Martin, A. P., & Richards, K. J. (2001). Mechanisms for vertical nutrient transport within a North Atlantic mesoscale eddy. *Deep Sea Research Part II: Topical Studies in Oceanography*, *48*(4), 757–773. https://doi.org/10.1016/S0967-0645(00)00096-5

McGillicuddy, D. J. (2016). Mechanisms of physical-biological-biogeochemical interaction at the oceanic mesoscale. *Annual Review of Marine Science*, *8*, 125–159. https://doi.org/10.1146/annurev-marine-010814-015606

McGillicuddy, D. J., Jr, Anderson, L. A., Bates, N. R., Bibby, T., Buesseler, K. O., Carlson, C. A., et al. (2007). Eddy/wind interactions stimulate extraordinary mid-ocean plankton blooms. *Science*, *316*, 1021–1026. https://doi.org/10.1126/science.1136256

McGillicuddy, D. J., & Robinson, A. (1997). Eddy-induced nutrient supply and new production in the Sargasso Sea. *Deep Sea Research Part I: Oceanographic Research Papers*, *44*(8), 1427–1450. https://doi.org/10.1016/s0967-0637(97)00024-1

McWilliams, J. C., & Yavneh, I. (1998). Fluctuation growth and instability associated with a singularity of the balance equations. *Physics of Fluids*, *10*(10), 2587–2596. https://doi.org/10.1063/1.869772

Montégut, C. D. B., Madec, G., Fischer, A. S., Lazar, A., & Iudicone, D. (2004). Mixed layer depth over the global ocean: An examination of profile data and a profile-based climatology. *Journal of Geophysical Research*, *109*(C12), C12003. https://doi.org/10.1029/2004JC002378

Moore, T. S., Matear, R. J., Marra, J., & Clementson, L. (2007). Phytoplankton variability off the western Australian coast: Mesoscale eddies and their role in cross-shelf exchange. *Deep Sea Research Part II: Topical Studies in Oceanography*, *54*, 943–960. https://doi.org/10.1016/j.dsr2.2007.02.006

Morrow, R., Birol, F., Griffin, D., & Sudre, J. (2004). Divergent pathways of cyclonic and anti-cyclonic ocean eddies. *Geophysical Research Letters*, *31*(24), L24311. https://doi.org/10.1029/2004GL020974

Nagai, T., Gruber, N., Frenzel, H., Lachkar, Z., McWilliams, J. C., & Plattner, G.-K. (2015). Dominant role of eddies and filaments in the offshore transport of carbon and nutrients in the California current system. *Journal of Geophysical Research*, *120*. https://doi.org/10.1002/2015JC010889

NASA-OB.DAAC. (2010). *SeaWiFS level-3 mapped Particulate Organic Carbon data version 2014 (S19972442010273.3m_MC_CHL_chlor_a_9km.nc) (1997–2010)*. NASA Goddard Space Flight Center, Ocean Ecology Laboratory, Ocean Biology Processing Group. Retrieved from http://oceandata.sci.gsfc.nasa.gov, https://doi.org/10.5067/ORBVIEW-2/SEAWIFS/L3M/POC/2014

NASA-OBPG. (2010). SeaWiFS data level-3 standard mapped image. (S19972442010273.3m_MC_CHL_chlor_a_9km.nc). NASA Goddard Space Flight Center, Ocean Ecology Laboratory, Ocean Biology Processing Group (1997–2010). Retrieved from http://oceandata.sci.gsfc.nasa.gov

NASA-OBPG. (2015). Defying fall weather to explore ocean ecosystems. (-NASA image by Norman Kuring, using VIIRS data from the Suomi National Polar-orbiting Partnership. Suomi NPP is the result of a partnership between NASA, the National Oceanic and Atmospheric Administration, and the Department of Defense. Photograph by Christien Laber, Rutgers University. Caption by Kathryn Hansen). Retrieved from https://earthobservatory.nasa.gov/IOTD/view.php?id=87140&eocn=image&eoci=related_image"

Oschlies, A., & Garçon, V. (1998). Eddy-induced enhancement of primary production in a model of the North Atlantic Ocean. *Nature*, *394*, 266–269. https://doi.org/10.1038/28373

Pegliasco, C., Chaigneau, A., & Morrow, R. (2015). Main eddy vertical structures observed in the four major eastern boundary upwelling systems. *Journal of Geophysical Research: Oceans*, *120*(9), 6008–6033. https://doi.org/10.1002/2015JC010950

Pelegrí, J. L., Arístegui, J., Cana, L., González-Dávila, M., Hernández-Guerra, A., Hernández-León, S., et al. (2005). Coupling between the open ocean and the coastal upwelling region off northwest Africa: Water recirculation and offshore pumping of organic matter. *Journal of Marine Systems*, *54*(1–4), 3–37. https://doi.org/10.1016/j.jmarsys.2004.07.003

Pelegrí, J. L., & Benazzouz, A. (2015). Coastal upwelling off northwest Africa. In L. Váldes & I. Déniz-González (Eds.), *Oeanographic and biological features in the Canary current large marine ecosystem (chap. 3.4)*. IOC-UNESCO. (Technical Series 115).

Qiu, B., & Chen, S. (2005). Eddy-induced heat transport in the subtropical North Pacific from Argo, TMI, and altimetry measurements. *Journal of Physical Oceanography*, *35*(4), 458–473. https://doi.org/10.1175/JPO2696.1

Renault, L., Molemaker, M. J., McWilliams, J. C., Shchepetkin, A. F., Lemarié, F., Chelton, D., et al. (2016). Modulation of wind work by oceanic current interaction with the atmosphere. *Journal of Physical Oceanography*, *46*(6), 1685–1704. https://doi.org/10.1175/jpo-d-15-0232.1

Reynolds, R. W., Smith, T. M., Liu, C., Chelton, D. B., Casey, K. S., & Schlax, M. G. (2007). Daily high-resolution-blended analyses for sea surface temperature. *Journal of Climate*, *20*, 5473–5496. https://doi.org/10.1175/2007JCLI1824.1

Ridgway, K. R., Dunn, J. R., & Wilkin, J. L. (2002). Ocean interpolation by four-dimensional least squares: Application to the waters around Australia. *Journal of Atmospheric and Oceanic Technology*, *19*, 1357–1375. https://doi.org/10.1175/1520-0426(2002)019<1357:oibfdw>2.0.co;2

Rio, M.-H., & Hernandez, F. (2004). A mean dynamic topography computed over the world ocean from altimetry, in situ measurements, and a geoid model. *Journal of Geophysical Research*, *109*(C12), C12032. https://doi.org/10.1029/2003JC002226

Samelson, R. M., Schlax, M. G., & Chelton, D. B. (2014). Randomness, symmetry, and scaling of mesoscale eddy life cycles. *Journal of Physical Oceanography*, *44*(3), 1012–1029. https://doi.org/10.1175/jpo-d-13-0161.1

Sangrà, P. (2015). Canary Islands eddies and coastal filaments off northwest Africa. In L. Váldes & I. Déniz-González (Eds.), *Oeanographic and biological features in the Canary current large marine ecosystem* (pp. 105–114). IOC-UNESCO. (Technical Series 115).

Sangrà, P., Pascual, A., Rodríguez-Santana, Á., Machín, F., Mason, E., McWilliams, J., et al. (2009). The canary eddy corridor: A major pathway for long-lived eddies in the subtropical North Atlantic. *Deep Sea Research I: Oceanographic Research Papers*, *56*(12), 2100–2114. https://doi.org/10.1016/j.dsr.2009.08.008

Schütte, F., Brandt, P., & Karstensen, J. (2016). Occurrence and characteristics of mesoscale eddies in the tropical northeastern Atlantic Ocean. *Ocean Science*, *12*(3), 663–685. https://doi.org/10.5194/os-12-663-2016

Seo, H., Miller, A. J., & Norris, J. R. (2016). Eddy-wind interaction in the California current system: Dynamics and impacts. *Journal of Physical Oceanography*, *46*(2), 439–459. https://doi.org/10.1175/JPO-D-15-0086.1

Shchepetkin, A. F., & McWilliams, J. C. (2005). The Regional Oceanic Modeling System (ROMS): A split-explicit, topographic-following-coordinate oceanic model. *Ocean Modeling*, *9*(4), 347–404. https://doi.org/10.1016/j.ocemod.2004.08.002

Siegel, D. A., McGillicuddy, D. J., & Fields, E. A. (1999). Mesoscale eddies, satellite altimetry, and new production in the Sargasso Sea. *Journal of Geophysical Research: Oceans*, *104*(C6), 13359–13379. https://doi.org/10.1029/1999JC900051

Stukel, M. R., Aluwihare, L. I., Barbeau, K. A., Chekalyuk, A. M., Goericke, R., Miller, A. J., et al. (2016). Mesoscale ocean fronts enhance carbon export due to gravitational sinking and subduction. *Proceedings of the National Academy of Sciences*, *114*(6), 1252–1257. https://doi.org/10.1073/pnas.1609435114

Thomas, L. N., Taylor, J. R., Ferrari, R., & Joyce, T. M. (2013). Symmetric instability in the gulf stream. *Deep Sea Research Part II: Topical Studies in Oceanography*, *91*, 96–110. https://doi.org/10.1016/j.dsr2.2013.02.025

Thompson, A. F., Heywood, K. J., Schmidtko, S., & Stewart, A. L. (2014). Eddy transport as a key component of the antarctic overturning circulation. *Nature Geoscience*, *7*(12), 879–884. https://doi.org/10.1038/ngeo2289

Vaillancourt, R. D., Marra, J., Seki, M. P., Parsons, M. L., & Bidigare, R. R. (2003). Impact of a cyclonic eddy on phytoplankton community structure and photosynthetic competency in the subtropical North Pacific Ocean. *Deep Sea Research Part I: Oceanographic Research Papers*, *50*(7), 829–847. https://doi.org/10.1016/s0967-0637(03)00059-1

Westberry, T., Behrenfeld, M. J., Siegel, D. A., & Boss, E. (2008). Carbon-based primary productivity modeling with vertically resolved photoacclimation. *Global Biogeochemical Cycles*, *22*(2), GB2024. https://doi.org/10.1029/2007gb003078

Yamamoto, A., Palter, J. B., Dufour, C. O., Griffies, S. M., Bianchi, D., Claret, M., et al. (2018). Roles of the ocean mesoscale in the horizontal supply of mass, heat, carbon, and nutrients to the Northern Hemisphere subtropical gyres. *Journal of Geophysical Research: Oceans*, *123*(10), 7016–7036. https://doi.org/10.1029/2018jc013969

Zhang, Z., Wang, W., & Qiu, B. (2014). Oceanic mass transport by mesoscale eddies. *Science*, *345*(6194), 322–324. https://doi.org/10.1126/science.1252418

Zhong, Y., & Bracco, A. (2013). Submesoscale impacts on horizontal and vertical transport in the gulf of Mexico. *Journal of Geophysical Research: Oceans*, *118*(10), 5651–5668. https://doi.org/10.1002/jgrc.20402

Zhong, Y., Bracco, A., Tian, J., Dong, J., Zhao, W., & Zhang, Z. (2017). Observed and simulated submesoscale vertical pump of an anticyclonic eddy in the south China Sea. *Scientific Reports*, *7*, 44011. https://doi.org/10.1038/srep44011